РОССИЙСКИЙ ГОСУДАРСТВЕННЫЙ ПЕДАГОГИЧЕСКИЙ УНИВЕРСИТЕТ им. А. И. ГЕРЦЕНА
HERZEN STATE PEDAGOGICAL UNIVERSITY of RUSSIA

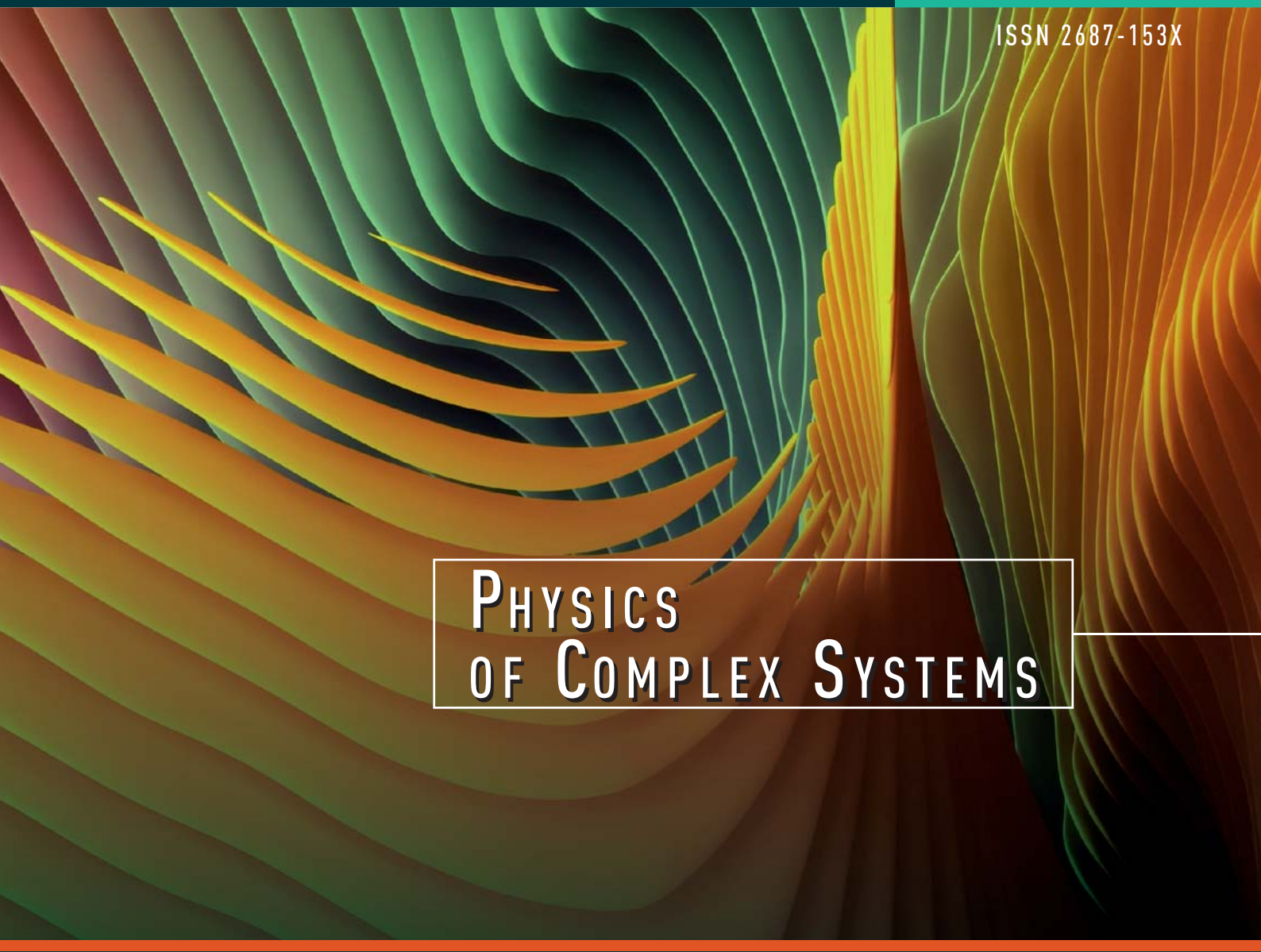

ISSN 2687-153X

Physics of Complex Systems

Т. 5 № 1 2024

Vol. 5 No. 1 2024

Herzen State Pedagogical University of Russia

ISSN 2687-153X (online)
physcomsys.ru
https://www.doi.org/10.33910/2687-153X-2024-5-1
2024. Vol. 5, no. 1

PHYSICS OF COMPLEX SYSTEMS

Mass Media Registration Certificate El No. FS77-77889, issued by Roskomnadzor on 10 February 2020
Peer-reviewed journal
Open Access
Published since 2020
4 issues per year

Publishing house of Herzen State Pedagogical University of Russia
48 Moika Emb., Saint Petersburg 191186, Russia
E-mail: izdat@herzen.spb.ru
Phone: +7 (812) 312-17-41

Data size 8,35 Mbyte
Published at 11.03.2024

Editor of the English text *K. Yu. Rybachuk*
Corrector *M. L. Kurakina*
Cover design by *O. V. Rudneva*
Layout by *D. V. Romanova*

CONTENTS

Condensed Matter Physics.
Physics of nanostructures.
Mesoscopic structures

UDC 535.5

EDN LFAWTO
https://www.doi.org/10.33910/2687-153X-2024-5-1-3-9

Three-photon absorption and photoluminescence in films of liquid-crystal polymers with embedded CdSe/ZnS quantum dots

V. Yu. Nesterov [1, 2], N. D. Presnov [1], S. V. Zabotnov [1], A. S. Merekalov [3], O. N. Karpov [1, 3], G. A. Shandryuk [1, 3], R. V. Talroze [1, 3], L. A. Golovan [✉1]

[1] Lomonosov Moscow State University, 1–2 Leninskie Gory, Moscow 119991, Russia
[2] Moscow Institute of Physics and Technology, 9 Institutsky Lane, Moscow 141701, Russian Federation
[3] A. V. Topchiev Institute of Petrochemical Synthesis, Russian Academy of Sciences, 29 Leninsky Ave., Moscow 119991, Russia

Authors

Vyacheslav Yu. Nesterov, e-mail: nesterovvy@my.msu.ru

Nikita D. Presnov, e-mail: presnovnikita@yandex.ru

Stanislav V. Zabotnov, ORCID: 0000-0002-2528-4869, e-mail: zabotnov@physics.msu.ru

Alexey S. Merekalov, ORCID: 0000-0002-8996-9568, e-mail: alexis@ips.ac.ru

Oleg N. Karpov, ORCID: 0000-0002-7314-7885, e-mail: o-karpov777@mail.ru

Georgiy A. Shandryuk, ORCID: 0000-0003-4349-5296, e-mail: shandgo@mail.ru

Raisa V. Talroze, ORCID: 0000-0002-9151-5493, e-mail: rtalroze@ips.ac.ru

Leonid A. Golovan, ORCID: 0000-0002-6838-5395, e-mail: golovan@physics.msu.ru

For citation: Nesterov, V. Yu., Presnov, N. D., Zabotnov, S. V., Merekalov, A. S., Karpov, O. N., Shandryuk, G. A., Talroze, R. V., Golovan, L. A. (2024) Three-photon absorption and photoluminescence in films of liquid-crystal polymers with embedded CdSe/ZnS quantum dots. *Physics of Complex Systems*, 5 (1), 3–9. https://www.doi.org/10.33910/2687-153X-2024-5-1-3-9 EDN LFAWTO

Received 8 December 2023; reviewed 10 January 2024; accepted 10 January 2024.

Funding: This work was supported by Russian Science Foundation project No. 23-19-00246, https://rscf.ru/project/23-19-00246/

Abstract. In this paper, we studied nonlinear absorption of infrared (IR) (1250 nm) femtosecond pulses and visible photoluminescence (PL) excited by them in liquid-crystal (LC) polymer films with embedded CdSe/ZnS core-shell type quantum dots (QDs). The dependence of nonlinear transmission on incident intensity indicated three-photon absorption in the films, with the three-photon absorption coefficient for the QD-LC polymer composite comparable with the one for bulk CdSe. The spectrum of PL excited by IR pulses coincides with one-photon excited PL spectrum. Dependence of the PL signal on the IR laser radiation power is cubic with further saturation for the spectral region from 2.10 to 2.25 eV, with saturation intensity decreasing with lower PL photon energy. The presence of the second-harmonic signal in the up-conversion spectrum results in its variation with an excitation power increase.

Keywords: semiconductor quantum dots, liquid-crystal polymer, up-conversion, photoluminescence, multiphoton absorption

Introduction

Nowadays, there is no need to prove the prospects of semiconductor quantum dots (QDs) or their applications in various fields. Strong restriction in charge carrier movements in the semiconductor nanoparticle significantly changes its electronic and optical properties (Efros, Brus 2021), opening up various ways of their usage in optoelectronics (Litvin et al. 2017), photovoltaics (Kirmani et al. 2020), laser generation (Jung et al. 2021), biomedical applications (Le et al. 2023), etc.

We should mention the use of the semiconductor QDs for up-conversion, i. e., light emission with wavelength below the excitation wavelength, among their highly promising applications (Rakovich, Donegan 2008). Up-conversion could be used for optical cooling (Ye et al. 2021), laser generation (Moon et al. 2021), infrared (IR) radiation detection (Zhou et al. 2020), bioimaging (Chen, Liang 2014) and therapy (Dutta, Barik 2022). Various mechanisms are responsible for up-converted PL, including population of defect states, phonon-assisted PL, two- and three-photon absorption (Laktaev et al. 2022; Wang et al. 2023), etc.

For many practical applications it would be useful to have a composite of semiconductor QDs and a transparent matrix that immobilizes them. Moreover, to ensure a maximal PL signal of the composite, QD concentration should be rather high, and ordered arrays of QDs should be formed. This can be done in a liquid-crystal (LC) polymer. When incorporated into the smectic LC structure, CdSe QDs break hydrogen bonds in the polymer, forming ionic bonds between polymeric carboxyl groups and QD surfaces, and nanolayers of QDs chemically bonded to the side chains of the macromolecules (Shandryuk et al. 2008). QD-polymer composites can contain up to 60 wt. % of QDs and demonstrate rather effective PL (Golovan et al. 2020; Tselikov et al. 2015). Transmission electron microscopy (TEM) data provides evidence of uniform QD distribution in composites (Shandryuk et al. 2008).

In this paper, we report on up-conversion in CdSe/ZnS core-shell QDs in a LC polymer and discuss the mechanism involved.

Experimental techniques

Samples

We used CdSe/ZnS core-shell QDs since they have more efficient PL and, in contrast to core-type CdSe QDs, core-shell QDs demonstrate mainly excitonic PL whereas the defect PL band is strongly suppressed (Golovan et al. 2020). The QDs were synthesized by means of a single-step synthetic method which helps to form a core/shell structure with a chemical composition gradient (Bae et al. 2008). The QDs were placed in a side chain acrylic LC polymer poly[4-(ω-acryloyloxyhexyloxy)benzoic acid] (BA-6PA). The QDs are built into a smectic layer with the thickness determined by the QD diameter. The structure of the initial LC polymer is retained for the QD fraction in the composite below a certain value (Shandryuk et al. 2008). The average diameter of the QDs is 4.8 nm with a standard deviation of 0.8 nm. A detailed description of the synthesis of QDs and LC polymer and the formation of composite films can be found elsewhere (Golovan et al. 2020). In our study we used 15-μm thick BA-6PA LC polymer films with embedded CdSe/ZnS QDs (20 and 40 wt. % concentration) and CdSe/ZnS QD suspension in toluene.

Optical measurements

Excitation of up-converted PL (UCPL) was carried out by radiation of a Cr:forsterite laser (Avesta-Project, Ltd, 1250 nm wavelength, 80 fs pulse duration, 1 nJ pulse energy, 80 MHz repetition rate). The radiation was focused on the film or in a cuvette with the QD suspension with a short-focus lens (focal length 7.5 mm, numerical aperture 0.3); the same lens was used to collect the PL signal, which was recorded with a Princeton Instrument Spectra Pro 2500i spectrometer equipped with a CCD array. UCPL spectra were compared with PL spectra excited by the second harmonic of radiation of a Nd:YAG laser EKPLA 2143A (532nm wavelength, 25 ns pulse duration, 10 Hz repetition rate) with photon energy over the QD bandgap. Laser radiation intensity at the samples in both cases did not exceed 10 GW/cm^2. Transmitting the excitation radiation through a gradient filter allowed it to be varied, which was used in obtaining dependences of the PL signals on the excitation intensity. The same short-focus lens and gradient filter were also used in a nonlinear-transmission measurement. Signals of IR radiation chopped at frequency 715 Hz incident on and transmitted through the LC polymer film with embedded 40 wt. % concentration of the QDs were detected by two diodes FD-10G and registered by two lock-in voltmeters SR 830.

 https://www.doi.org/10.33910/2687-153X-2024-5-1-3-9

Results and discussion

The PL spectra excited by IR femtosecond radiation in the composites containing 20 and 40 wt. % of the QDs and in the QD suspension in toluene are shown in Fig. 1. The PL spectra width is explained by QD size distribution. One can see a red shift of the PL spectra with an increase in QD concentration.

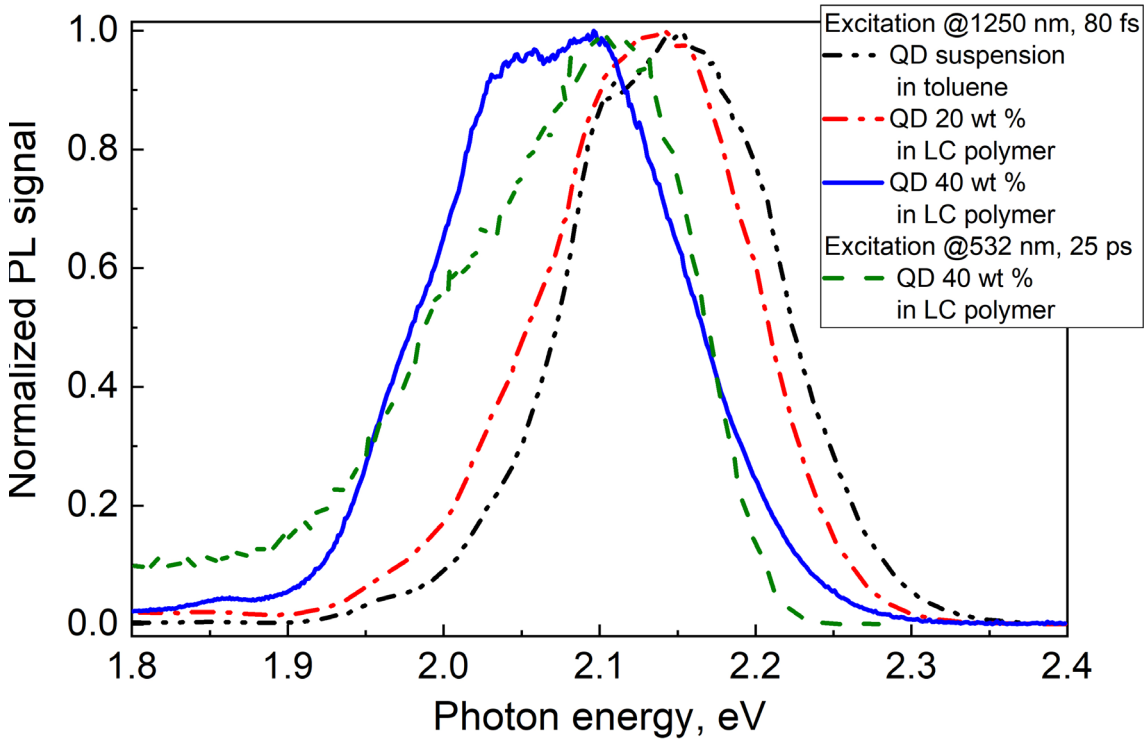

Fig. 1. Normalized PL spectra for the composites containing 20 wt. % (dot-dash line) and 40 wt. % (solid line) of the QDs and the QD suspension in toluene (dot-dot-dash) excited by IR femtosecond pulses and for PL spectra excited by picosecond laser radiation at wavelength of 532 nm (dash line)

The effect can be explained by an energy transfer from smaller QDs to bigger QDs, which emits photons of less energy due to their smaller band gaps. The PL spectra excited by femtosecond pulses at 1250 nm and by picosecond pulses at 532 nm are very close. It is worth noting that the PL spectra are not excited by continuous-wave laser radiation at 1250 nm and the same and even higher average power, which shows that PL emission depends on excitation radiation intensity, not power.

The UCPL spectrum strongly depends on focusing the IR laser beam at the surface of the sample (Fig. 2). We should mention that for the used laser beam the waist radius w_0 is 6 μm and Rayleigh length (distance where the beam section is twice the size at the waist) $\pi w_0^2 / \lambda$, where λ is wavelength, is 90 μm, which significantly exceeds the film thickness. The maximal PL signal is achieved when the laser beam waist is at the film surface, as confirmed by the maximum of the third-harmonic signal. Further displacement of the beam focal region inside the sample results in a UCPL signal decrease and red shift of its maximum. These facts can be explained by the reabsorption of the PL emitted inside the film.

To establish the UCPL mechanism, it would be instructive to study specific properties of laser radiation absorption by the films of the LC polymer with embedded QDs and obtain a dependence of the PL spectra on excitation power.

An experiment on the femtosecond IR pulse transmission through the LC polymer film with 40 wt. % concentration of the QDs demonstrates a transmittance decrease with an incident radiation intensity increase (Fig. 3, inset). The PL photon energy can exceeds the excitation photon energy more than twice, which is why three-photon absorption can be supposed to excite UCPL. Indeed, in the simplest case of the only three-photon absorption in the medium, transmission of intensity I along the coordinate z inside the medium is governed by the equation:

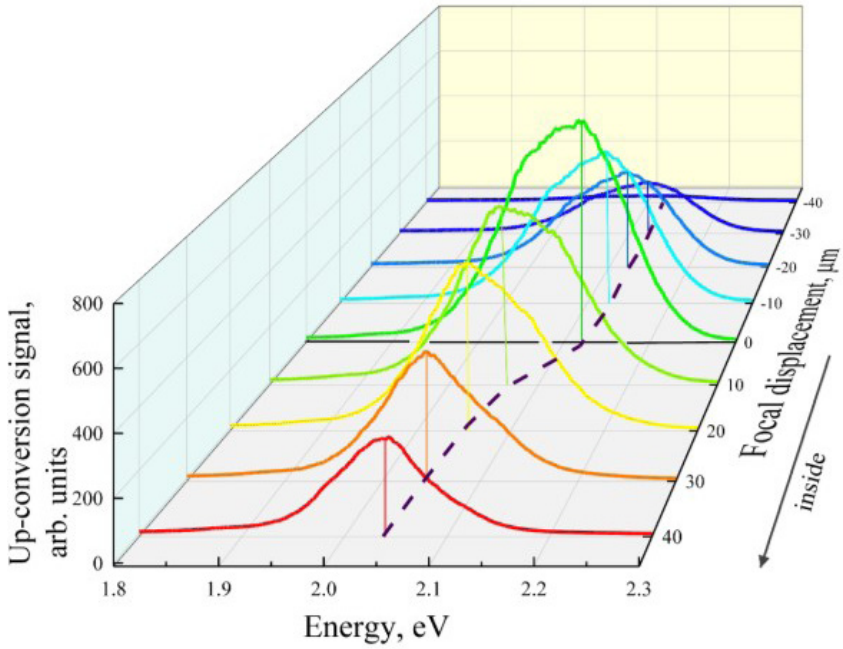

Fig. 2. Variation of the UCPL spectrum with the movement of the excitation beam focus

$$\frac{dI}{dz} = -\gamma I^3 \ , \tag{1}$$

where γ is a three-photon absorption coefficient. From Eq. 1 one can conclude the following ratio:

$$\frac{T_0^{\,2}}{T^2} = 1 + 2\gamma d I_0^{\,2} \ , \tag{1}$$

where d is film thickness, I_0 is intensity of incident radiation, T is transmittance at intensity I_0, while T_0 is film transmittance at very low radiation intensity.

Fig. 3 presents the obtained dependence of the $T_0^{\,2}/T^2$ value on $I_0^{\,2}$. Nonlinear absorption effects are noticeable for intensity above 10 MW/cm^2, and Eq. 2 is in line with experimental data. This allows us to estimate the three-photon absorption coefficient γ, which was found to be equal to 0.17 cm^3/W^2. Although the QD volume fraction in the composite film is about 0.09, the γ value obtained for it is comparable with the one for bulk semiconductors (0.13–0.24 cm^3/W^2 @ 1.54 μm for CdSe and 0.0017 cm^3/W^2 @ 1.06 μm for ZnS (Benis et al. 2020)). Thus, we can conclude that UCPL is caused by the three-photon absorption of the IR femtosecond radiation.

The dependence of the UCPL signal on laser radiation power would also be very instructive. The PL signal excited by radiation at wavelength of 532 nm shows linear dependence on the laser radiation power. For the used intensities it does not demonstrate any significant saturation.

Fig. 4 presents UCPL spectra of the QD suspension in toluene and QDs embedded into the LC polymer with a concentration of 40 wt. % obtained at different average excitation radiation power P_{exc}. In the latter case, one can see a significant UCPL spectrum variation with an increase of the excitation radiation power (Fig. 4c), whereas for the QD suspension in toluene variations are much less pronounced (Fig. 4a).

This fact makes it necessary to follow changes of a separate spectral component of the UCPL signal (1.95, 2.00, 2.05, 2.10, 2.15, 2.20 and 2.25 eV) with excitation power variations. For more clarity, we normalize them by the ones for lower power intensity (15 mW for the QD toluene suspension and 7 mW for the composite of QDs and LC polymer) (Figs. 4b, 4d). As one can see, these dependences are very close for both media. UCPL signals in the spectral region from 2.10 to 2.25 eV demonstrate cubic dependence on the P_{exc} value below 50 mW (intensity of 7 GW/cm^2); for higher excitation power the UCPL signal tends towards saturation. Saturation of the UCPL signal at 2.05 eV starts at a much lower P_{exc} value (20 mW). This fact could be due to an energy transfer from smaller QDs with a higher band gap to bigger

 https://www.doi.org/10.33910/2687-153X-2024-5-1-3-9

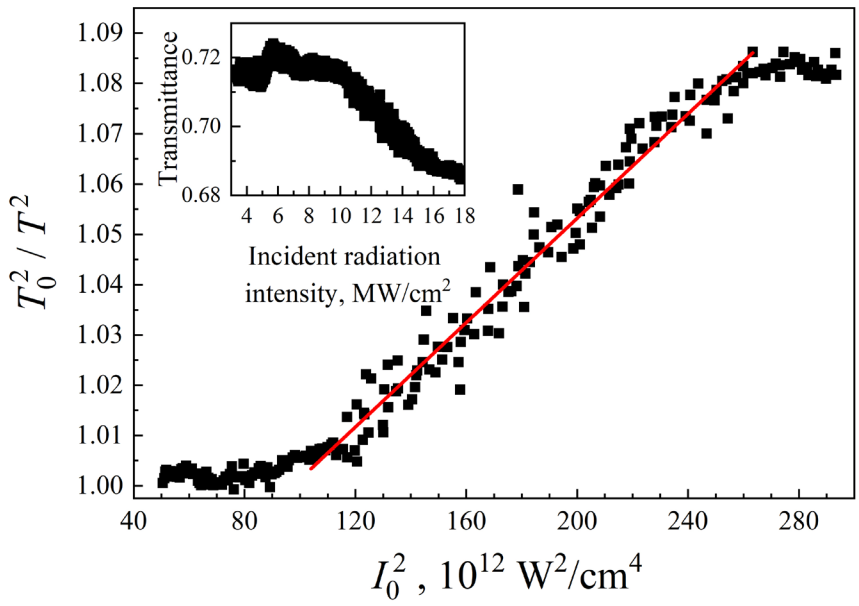

Fig. 3. T_0^2/T^2 vs. I_0^2. The line is an approximation of dependence according to Eq. 2. The inset is dependence of the LC film with embedded QDs (40 wt. %) transmittance on intensity of incident femtosecond pulses at wavelength of 1250 nm

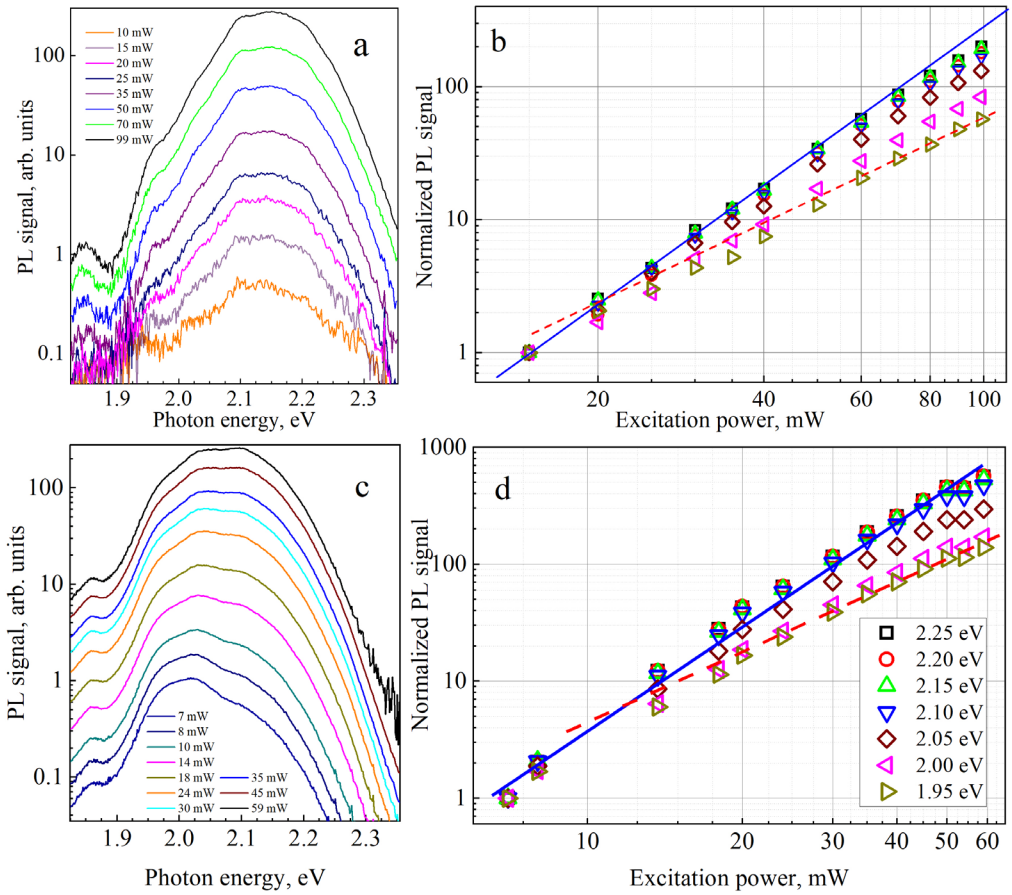

Fig. 4. UCPL spectra for the QD suspension in toluene (a) and QDs embedded into the LC polymer (40 wt. %) (c) and dependences of UCPL spectral components at different photon energies normalized by spectral components taken for the same photon energy at P_{exc} = 15 mW for the QD suspension in toluene (b) and by spectral components at P_{exc} = 7 mW for the QDs embedded into the LC polymer (40 wt. %) (d) on average excitation radiation power. Solid and dashed lines correspond to the cubic and quadratic dependences of the UCPL signal on P_{exc}

QDs with a lower band gap. At least, the UCPL spectral components in the region 1.95 to 2.00 eV demonstrate their quadratic dependence on P_{exc} for the excitation power above 20 mW. It is worth noting that this spectral range corresponds to the second-harmonic generated by the Cr:forsterite laser radiation. Thus, we can conclude that a part of the UCPL spectrum for QDs embedded into the LC polymer is the second harmonic spectrum generated in QDs, which results in variation of the UCPL spectrum with variations of the excitation power. Since the concentration of the QDs in the suspension is obviously lower than in the LC polymer-QD composite, the second-harmonic spectrum is less pronounced in the former medium.

Conclusions

We demonstrated that the up-conversion signal generated both in a suspension of CdSe/ZnS quantum dots in toluene and in a composite film of quantum dots and a liquid-crystal polymer under excitation by femtosecond infrared (1250 nm) pulses is caused by three-photon absorption. A nonlinear transmission measurement allowed us to find the three-photon absorption coefficient for the LC polymer composite with 40 wt. % QD concentration, with the value comparable to the one for bulk CdSe. The dependence of the up-conversion signal in the spectral range 2.10 to 2.25 eV on the average excitation radiation power is cubic and tends towards saturation, whereas for the spectral range 1.95 to 2.00 eV, which is the region of the second harmonic of the excitation radiation, the up-converted signal demonstrates quadratic dependence on the excitation radiation power. As a result, in a composite film with rather high QD concentration, the up-conversion spectrum varies with excitation variation.

Conflict of Interest

The authors declare that there is no conflict of interest, either existing or potential.

Author Contributions

The authors have made an equal contribution to the paper.

References

Bae, W. K., Char, K., Hur, H., Lee, S. (2008) Single-step synthesis of quantum dots with chemical composition gradients. *Chemistry of Materials*, 20 (2), 531–539. https://doi.org/10.1021/cm070754d (In English)

Benis, S., Cirloganu, C., Cox, N. et al. (2020) Three-photon absorption spectra and bandgap scaling in direct-gap semiconductors. *Optica*, 7 (8), 888–899. https://doi.org/10.1364/OPTICA.396056 (In English)

Chen, Y., Liang, H. (2014) Applications of quantum dots with upconverting luminescence in bioimaging. *Journal of Photochemistry and Photobiology B: Biology*, 135, 23–32. https://doi.org/10.1016/j.jphotobiol.2014.04.003 (In English)

Dutta, R., Barik, P. (2022) Upconversion and downconversion quantum dots for biomedical and therapeutic applications. In: P. Barik, S. Monal (eds.). *Application of quantum dots in biology and medicine. Recent advances*. Singapore: Springer Publ., pp. 229–263. https://doi.org/10.1007/978-981-19-3144-4_12 (In English)

Efros, A. L., Brus, L. E. (2021) Nanocrystal quantum dots: From discovery to modern development. *ACS Nano*, 15 (4), 6192–6210. https://doi.org/10.1021/acsnano.1c01399 (In English)

Golovan, L. A., Elopov, A. V., Zaitsev, V. B. et al. (2020) Photoluminescence of CdSe and CdSe/ZnS quantum dots in amorphous and liquid-crystalline polymer matrices. *Polymer Science. Series A: Physics*, 62 (6), 701–713. http://dx.doi.org/10.1134/S0965545X20060048 (In English)

Jung, H., Ahn, N., Klimov, V. I. (2021) Prospects and challenges of colloidal quantum dot laser diodes. *Nature Photonics*, 15 (9), 643–655. https://doi.org/10.1038/s41566-021-00827-6 (In English)

Kirmani, A. R., Luther, J. M., Abolhasani, M., Amassian, A. (2020) Colloidal quantum dot photovoltaics: Current progress and path to gigawatt scale enabled by smart manufacturing. *ACS Energy Lett*ers, 5 (9), 3069–3100. https://doi.org/10.1021/acsenergylett.0c01453 (In English)

Laktaev, I. D., Saidzhonov, B. M., Vasiliev, R. B. et al. (2022) Two-photon excited biexciton photoluminescence in colloidal nanoplatelets CdSe/CdS. *Journal of Luminescence*, 252, article 119414. https://doi.org/10.1016/j.jlumin.2022.119414 (In English)

Le, N., Kim, K. (2023) Current advances in the biomedical applications of quantum dots: Promises and challenges. *International Journal of Molecular Science*, 24 (16), article 12682. https://doi.org/10.3390/ijms241612682 (In English)

Litvin, A. P., Martynenko, I. V., Purcell-Milton, F. et al. (2017) Colloidal quantum dots for optoelectronics. *Journal of Material Chemistry A*, 5 (26), 13252–13275. https://doi.org/10.1039/C7TA02076G (In English)

Moon, B.-S., Lee, T. K., Jeon, W. C. et al. (2021) Continuous-wave upconversion lasing with a sub-10 W cm^{-2} threshold enabled by atomic disorder in the host matrix. *Nature Communications*, 12 (1), article 4437. https://doi.org/10.1038/s41467-021-24751-z (In English)

Rakovich, Yu. P., Donegan, J. F. (2008) Anti-Stokes photoluminescence in semiconductor nanocrystal quantum dots. In: A. L. Rogach (ed.). *Semiconductor nanocrystal quantum dots*. Vienna: Springer Publ., pp. 257–275. http://dx.doi.org/10.1007/978-3-211-75237-1_9 (In English)

Shandryuk, G. A., Matukhina, E. V., Vasil'ev, R. B. et al. (2008) Effect of H-bonded liquid crystal polymers on CdSe quantum dot alignment within nanocomposite. *Macromolecules*, 41 (6), 2178–2185. http://dx.doi.org/10.1021/ma701983y (In English)

Tselikov, G. I., Timoshenko, V. Yu., Golovan, L. A. et al. (2015) Role of the polymer matrix on the photoluminescence of embedded CdSe quantum dots. *ChemPhysChem*, 16 (5), 1071–1078. http://dx.doi.org/10.1002/cphc.201402913 (In English)

Wang, F., He, M., Huang, B. et al. (2023) Band gap engineering improves three-photon luminescence of quantum dots for deep brain imaging. *Analytical Chemistry*, 95 (29), 10947–10956. https://doi.org/10.1021/acs.analchem.3c00845 (In English)

Ye, Z., Lin, X., Wang, N. et al. (2021) Phonon-assisted up-conversion photoluminescence of quantum dots. *Nature Communications*, 12 (1), article 4283. https://doi.org/10.1038/s41467-021-24560-4 (In English)

Zhou, W., Shang, Y., García de Arquer, F. P. et al. (2020) Solution-processed upconversion photodetectors based on quantum dots. *Nature Electronics*, 3 (5), 251–258. https://doi.org/10.1038/s41928-020-0388-x (In English)

Condensed matter physics.
Dielectric

UDC 538.9

EDN GUXCPV
https://www.doi.org/10.33910/2687-153X-2024-5-1-10-17

Dielectric properties of photoanodes for dye-sensitized solar cells

E. V. Tekshina ✉[1], P. I. Lazarenko [2], A. S. Steparuk [3], D. A. Krupanova [2], S. A. Kozyukhin [1]

[1] Kurnakov Institute of General and Inorganic Chemistry, 31 Leninsky Ave., Moscow 119991, Russia
[2] National Research University of Electronic Technology, 1 Shokina Str., Zelenograd 124498, Russia
[3] I. Ya. Postovsky Institute of Organic Synthesis of the Ural Branch of the Russian Academy of Sciences, 22/20 Sofia Kovalevskaya Str., Ekaterinburg 20137, Russia

Authors

Ekaterina V. Tekshina, ORCID: 0009-0000-0308-4228, e-mail: ekaterina3141@mail.ru

Petr I. Lazarenko, ORCID: 0000-0003-4309-3481, e-mail: aka.jum@gmail.com

Alexander S. Steparuk, ORCID: 0000-0003-3235-4674, e-mail: steparuk96@mail.ru

Darya A. Krupanova, ORCID: 0000-0003-3278-7664, e-mail: krupanova.d@gmail.com

Sergey A. Kozyukhin, ORCID: 0000-0002-7405-551X, e-mail: sergkoz@igic.ras.ru

For citation: Tekshina, E. V., Lazarenko, P. I., Steparuk, A. S., Krupanova, D. A., Kozyukhin, S. A. (2024) Dielectric properties of photoanodes for dye-sensitized solar cells. *Physics of Complex Systems*, 5 (1), 10–17. https://www.doi.org/10.33910/2687-153X-2024-5-1-10-17 EDN GUXCPV

Received 27 December 2023; reviewed 19 January 2024; accepted 26 January 2024.

Funding: This work was supported by the Russian Science Foundation (project No. 22-73-00291, dyes fabrication). EVT acknowledges the support of the Ministry of Science and Higher Education of the Russian Federation as part of the State Assignment of the Kurnakov Institute of General and Inorganic Chemistry of the Russian Academy of Sciences in sample design.

Abstract. Solar energy (SE) research is relevant today, especially as far as dye-sensitized solar cells (DSSC) are concerned, which are third-generation devices. The prospect of their future development lies in the creation of architectural and interior-integrated panels, flexible and portable devices for SE conversion. Examining the properties of their components and their mutual impact is crucial for improving the efficiency of DSSC and moving away from the standard cell design.

In this work, we investigated dielectric properties of photoanodes (PhA) for DSSC. The influence of a dye on dielectric properties of PhA is shown. By measuring dielectric properties in the samples, we obtained dielectric permittivity and dielectric loss tangent that ranged from −50 to 150 °C and from 10^{-1} to 10^{6} Hz. Our results make a significant contribution towards a better understanding of the influence that the dye has on dielectric properties of PhA and can serve to develop new efficient composite materials for new-generation photoelectronic devices.

Keywords: dielectric properties, mesoporous layer, titanium dioxide, dye-sensitized solar cells, composite materials, organic dyes

Introduction

A growing interest in DSSC witnessed since 1991 (O'Regan, Grätzel 1991) is a result of its low production cost, extended service life, ability to work under poor or artificial lighting, transparency and mechanical strength. The combination of properties and color solutions makes DSSC a viable alternative power source for architectural-integrated photovoltaic systems (Szindler et al. 2021) and portable electronics, which can help to support the concept of the 'internet of things' (Kim, Han 2020).

Standard device design includes a photoanode (PhA) and a photocathode with an electrolyte between them. The PhA is conductive-coated glass (FTO or ITO) with a semiconductor porous layer of metal oxide on it, which is sensitized by a dye.

The primary problem with DSSC is that it is not as efficient as silicon solar cells, but this issue can be solved by optimizing devices, expanding their applications and scaling them.

Scaling is economically profitable, but it can be even more profitable to replace an expensive metal-containing dye with an organic one, which has a much lower cost. Since titanium dioxide material is a semiconductor, which negatively affects the operation of the device, the impact of adding organic material on the conductivity of material is yet to be determined. We should thus examine the impact of the organic dye on the semiconductor layer and dielectric properties of the photoanode.

Given interaction between functional layers in DSSC devices, it is important to study their properties in both ways: independently and synthesized multiple components.

Dielectric properties are affected by microstructural features such as grain size, porosity, secondary phases, impurities and structural defects (point defects and cracks). However, most of the work on dielectric properties of titanium dioxide in its different modifications (rutile, brookite, anatase) refers to powders or compressed samples (Bonkerud et al. 2021; Wypych et al. 2014). Another question is how a metal-free dye affects dielectric properties of materials in devices.

Given all the above, it makes sense to research dielectric properties for DSSC, where TiO_2 is used as a mesoporous layer in PhA, and to conduct dielectric studies directly on PhA, both with and without dyes.

Thus, this work aims to study the dielectric properties of PhA and investigate the influence of dyes on these properties.

Methods and materials

The work was researched by PhA for DSSC. PhA has a multilayer structure: a glass substrate with a conductive coating, with a semiconductor mesoporous layer of metal oxide applied, which can be sensitized by various dyes. Ti-Nanoxide T/SP, particle size 15–20 nm (Solaronix), fluorine-doped tin oxide (FTO) coated glasses, 20 × 20 mm, (Solaronix) were used. To obtain samples of titanium dioxide films on glass with a conductive coating, we applied the 'doctor blade' paste technique (Berni et al. 2004), active area 6 × 6 mm. Step-by-step heating and extracting at 450 °C were used, which ensured gradual removal of the solvent both from the surface of the layer and from its volume, thus avoiding stresses and cracking. Chloroform dye solutions $c = 5 \times 10^{-4}$ mol/l were made for sensitization of the titanium dioxide layer. After that the glass with the pre-formed film was placed in this solution with an exposure of t = 24h. The photoanode was then extracted from the solution and dried at room temperature in the air. Organic D-π-A dyes IS5 and IS10, synthesized and investigated earlier (Steparuk et al. 2022), were chosen for the survey. These dyes have a thieno[3,2-*b*]indole nucleus, electrodonor part. The main distinction is the acceptor group: 2-cyanoacryl acid in IS5 and 5-(methylene) barbiturate acid in IS10.

Dielectric measurements were carried out by a Novocontrol Technologies 'Concept-81' spectrometer (Novocontrol Technologies GmbH & Co. KG, Montabaur, Germany; 'Modern physical and chemical methods of formation and study of materials for the needs of industry, science and education', Herzen University). In order to measure the dielectric properties of the mesoporous layer of titanium dioxide in the form used in DSSC, an attachment has been made to allow direct measurement of the PhA (Fig. 1). This attachment (holder) was needed to measure the porous film (thickness of the μm order) on the glass, precisely as the materials are used in DSSC devices.

We used parallel plate measurement. The measuring design is a capacitor with the measured material placed between the plates. When the formed samples are measured, the contact area and thickness of the measured layer is the same. Temperature measurement ranges from –50 to 150 °C, and frequencies vary from 10^{-1} to 10^{6} Hz.

Results and discussions

Dielectric permittivity describes the interaction of the material with the electric field and is a complex quantity:

$$\varepsilon^* = \varepsilon' + \varepsilon'' \quad (1)$$

where ε' and ε'' are the real part and the imaginary one, respectively. The ε' value shows how much of external electric field energy is stored in the material. The imaginary part of permittivity ε'' is called the loss factor and shows the level of dissipation or loss of the external electric field in the material. Figures 2a-c show the temperature-frequency dependencies of ε' measured for the non-sensitized PhA (2a) and PhA with a dye (2b, c).

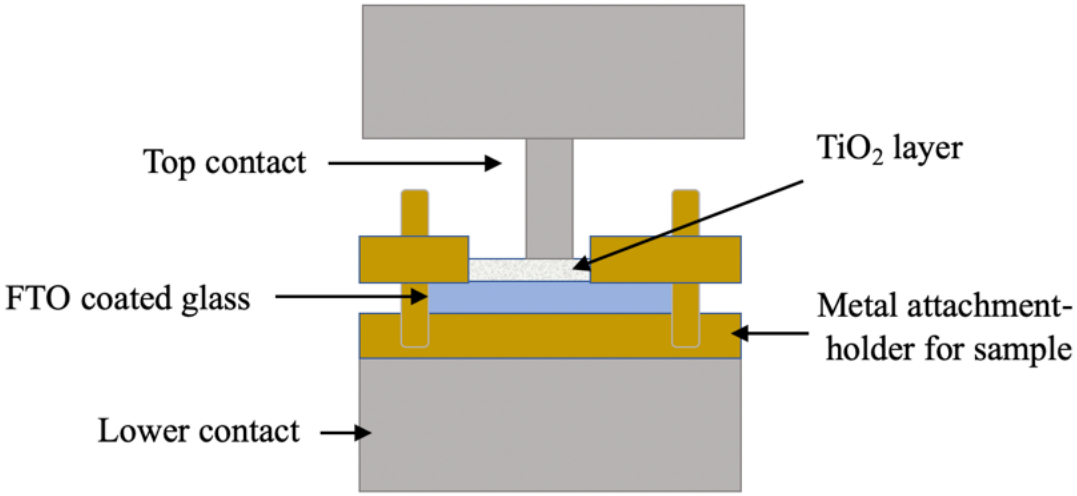

Fig. 1. Diagram of the cell for measuring the dielectric properties of the titanium dioxide film formed on FTO conductive glass

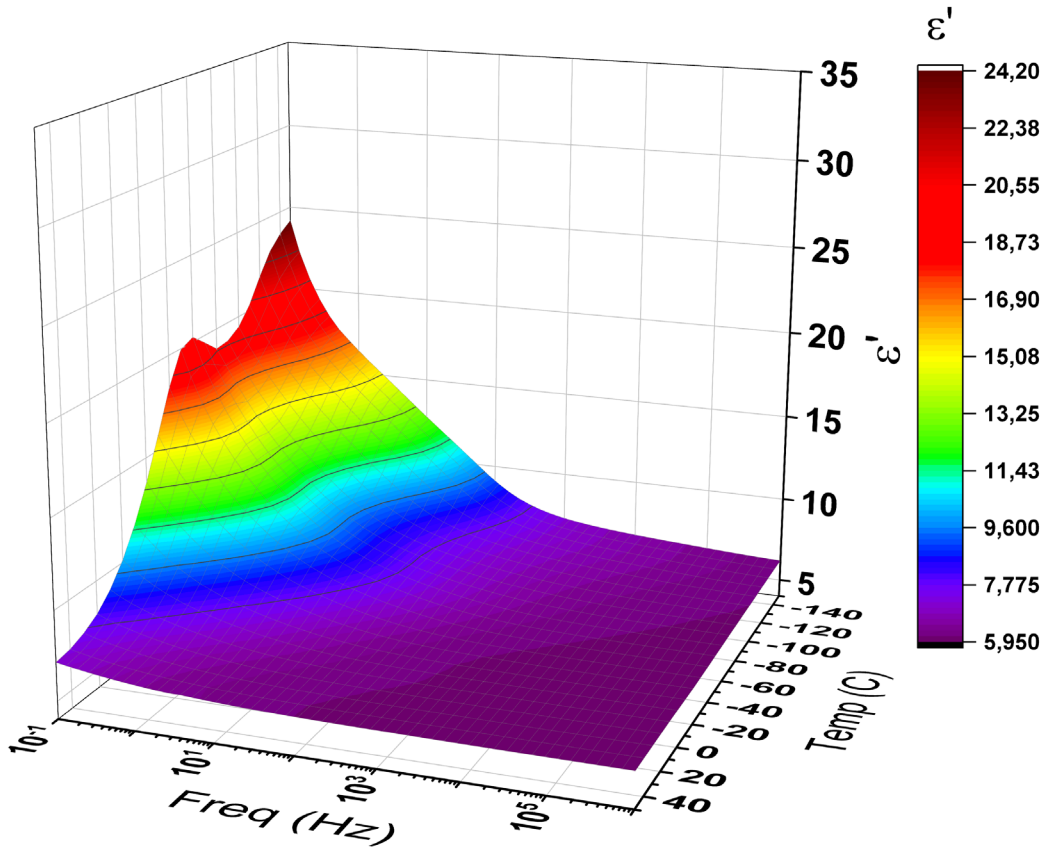

Fig. 2a. Temperature-frequency graphs of the real part of permittivity measured for the PhA without dyes

https://www.doi.org/10.33910/2687-153X-2024-5-1-10-17

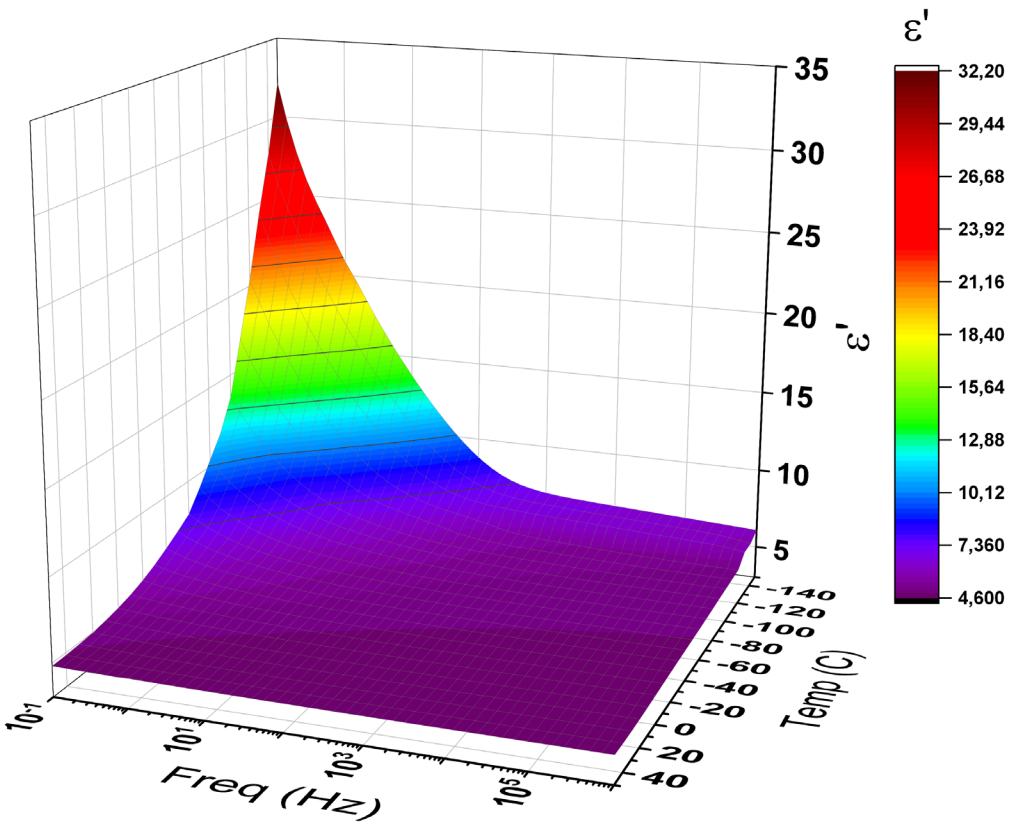

Fig. 2b Temperature-frequency graphs of the real part of permittivity measured for the PhA sensitized by the IS5 dye

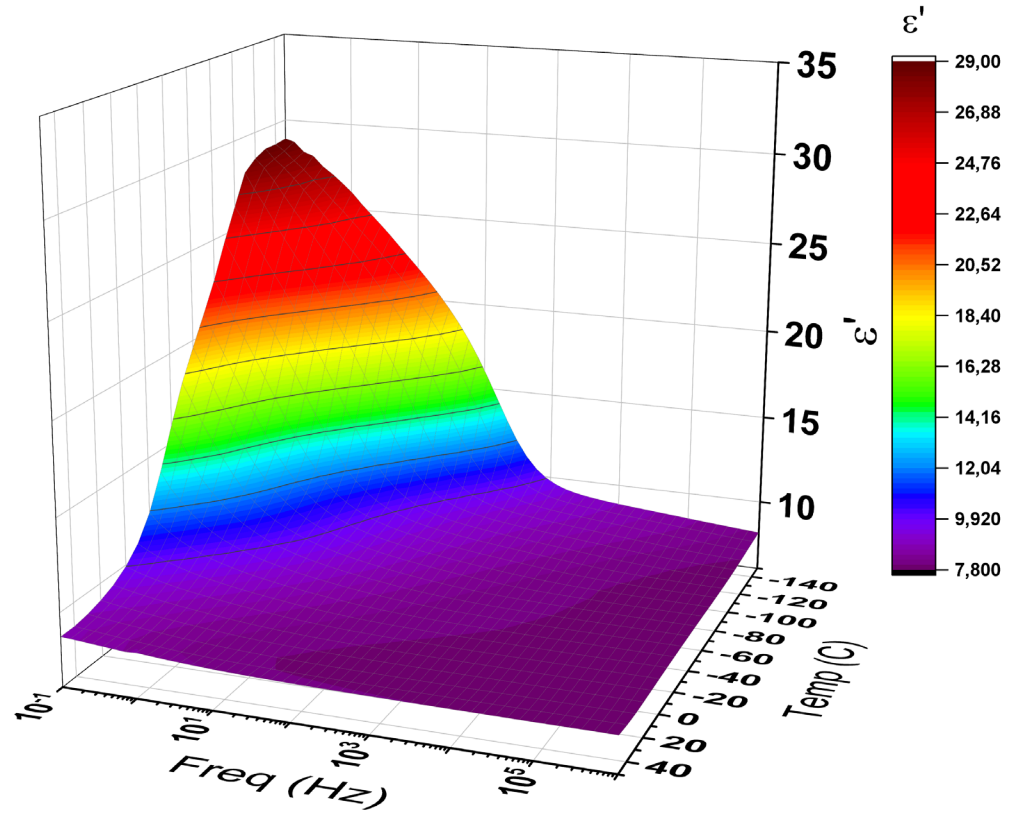

Fig. 2c Temperature-frequency graphs of the real part of permittivity measured for the PhA sensitized by the IS10 dye

The graphs show that frequency increases (to about 10^3 Hz), permittivity decreases while significant dispersion is observed only in the region of negative temperature. Meanwhile, changes are insignificant in the temperature range close to room temperature. Similar effect for metal oxides was discussed in another article (Wang et al. 2006). Reduced permittivity with increased frequency is observed here due to dielectric relaxation since the speed of rotation of the dipole at high frequency is not enough to match the displacement of the applied variable voltage. This may be due to the fact that in this material electrical response is complex and consists mainly of contributions of polarization from different molecular levels and polarization of the space charge. It should also be noted that the studied titanium dioxide consisting of nanocrystals is porous and really represents the system consisting of a mixture of a semiconductor and air. The values of the ε' titanium dioxide-dye system (Figure 2b, c) differ from the pure TiO_2 layer (Figure 2a) at all frequencies due to the dipole-dipole interaction when adding fillers as organic dyes. It also shows that dielectric properties of such composites can be regulated by varying the type and concentration of the filling agent (Huang et al. 2005). The combined Maxwell-Wagner-Sillars effect has its own dipole polarization, and polarization on the inner surfaces of the polarization section explains this difference (Ramesan 2015). It can also be seen that after the dye is added, polarization in the material decreases with an increase in frequency faster than in the dye-free material. This may indicate a cumulative increase in the rotation rate of dipoles in the material and a global deterioration in the ability of the system to store energy from the external electric field. However, it may also indicate an increase in the conductivity of the composite material. It is important to note that there is a difference in the influence of dyes with different anchor groups on the behavior of the system. For the IS5 dye there is only a faster decrease in the ε value with increasing frequency, and in the case of the IS10 dye, we see the preservation of the value of the actual polarization component at low frequencies and only after increasing frequency, that is, in this range, does the system better accumulate the energy of the external electric field. We can conclude that the dye carrying 5-(methylene) barbituric acid as an anchor group makes a greater change in the dielectric properties of the system which indirectly indicates its better ability to fit into pores of TiO_2 film.

The tangent of dielectric loss tan (δ) was determined by:

$$\tan(\delta) = \frac{\varepsilon''}{\varepsilon'} \quad (2)$$

Assuming that dielectric loss is caused by polarization, the graph will show a maximum, which is observed in all samples for high temperatures 130–150 °C for pure titanium dioxide (Fig. 3) and dye-sensitized one (IS5) (Fig. 3a), and 90–150 °C for titanium dioxide with the IS10 dye as a sensitizer (Fig. 3b,c). After sensitization, the value of the dielectric loss tangent increases slightly, which may be due to denser packaging because the semiconductor oxide matrix contains dye molecules and there is friction when the dipoles are rotated by an external electric field, which also effects the value. It should be noted that the contribution of this type of loss is small, and the increase in loss is small, accordingly. There is also a downward trend in losses as the frequency increases after the maximum loss as dipoles and ions do not have time to rotate or shift following the frequency of the electric field, and therefore losses are reduced. The maximum loss for the pure TiO_2 film and IS5-dye-sensitive TiO_2 film is at 10^2, and in the case of sensitization by the IS10 dye carrying 5-(methylene) barbituric acid as an anchor group, shifts to a value close to 10^3 Hz for temperatures 100–150 °C. The relaxation phenomenon indicated by the arrow in the tangent image of the loss angle tan (δ) for all cases (Fig. 3, 3a, 3b) may be related to energy dissipation at grain boundaries or/and electrode influence (Mohamed et al. 2011; Romeu et al. 2013). Higher tan(δ) values at higher frequencies may be associated with spatial charge polarization with the addition of a dye, macroscopic distortion and higher interphase polarization (Huang et al. 2005).

Conclusions

We studied nanocrystalline titanium dioxide layers used as photoanodes for DSSC, both with dye molecules in TiO_2 pores and without. Supplementation of a titanium dioxide matrix with an organic dye has been proven to affect dielectric properties. Specifically, organic dyes contribute to the dipole-dipole interaction, which reduces the values of permittivity at all frequencies, compared to the pure material, which may affect the capacity of the DSSC device itself. Changes in permittivity and the dielectric loss tangent also depend on the type of the dye incorporated into the system, which indicates the ability

 https://www.doi.org/10.33910/2687-153X-2024-5-1-10-17

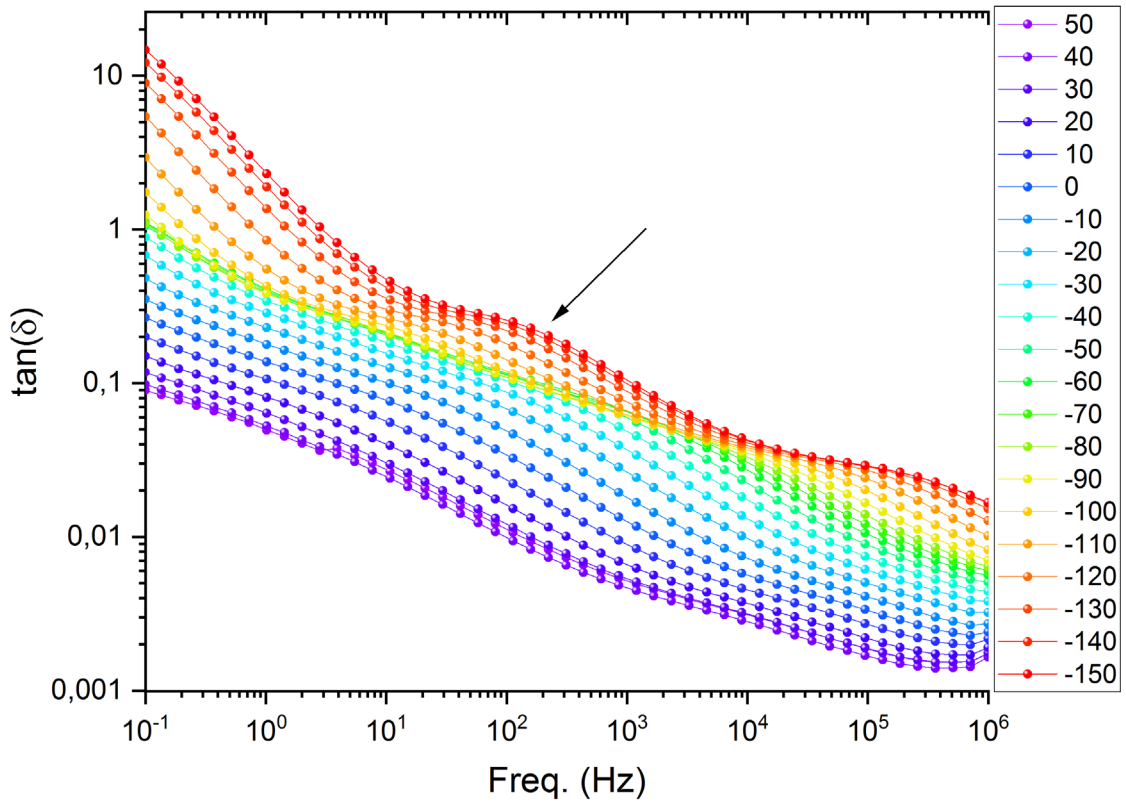

Fig. 3a. Frequency dependence of the tangent of dielectric loss tan (δ) measured at different temperatures for the PhA without dyes

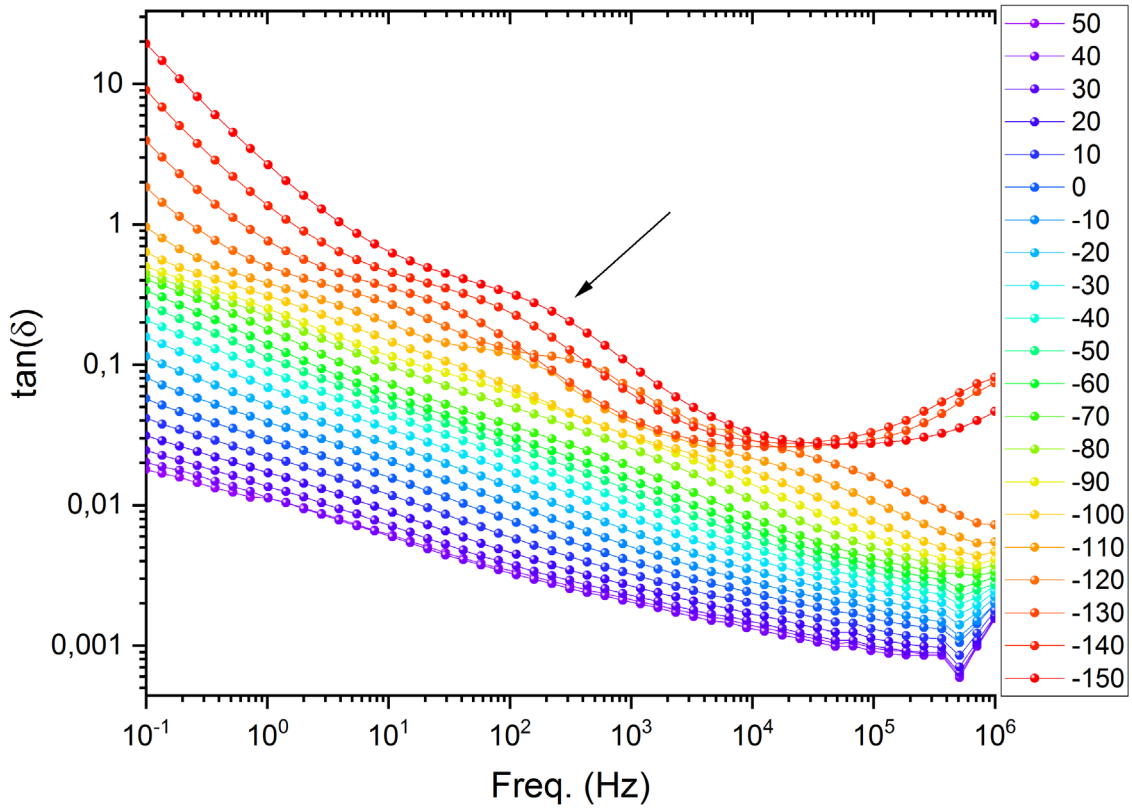

Fig. 3b. Frequency dependence of the tangent of dielectric loss tan (δ) measured at different temperatures for the PhA sensitized by the IS5 dye

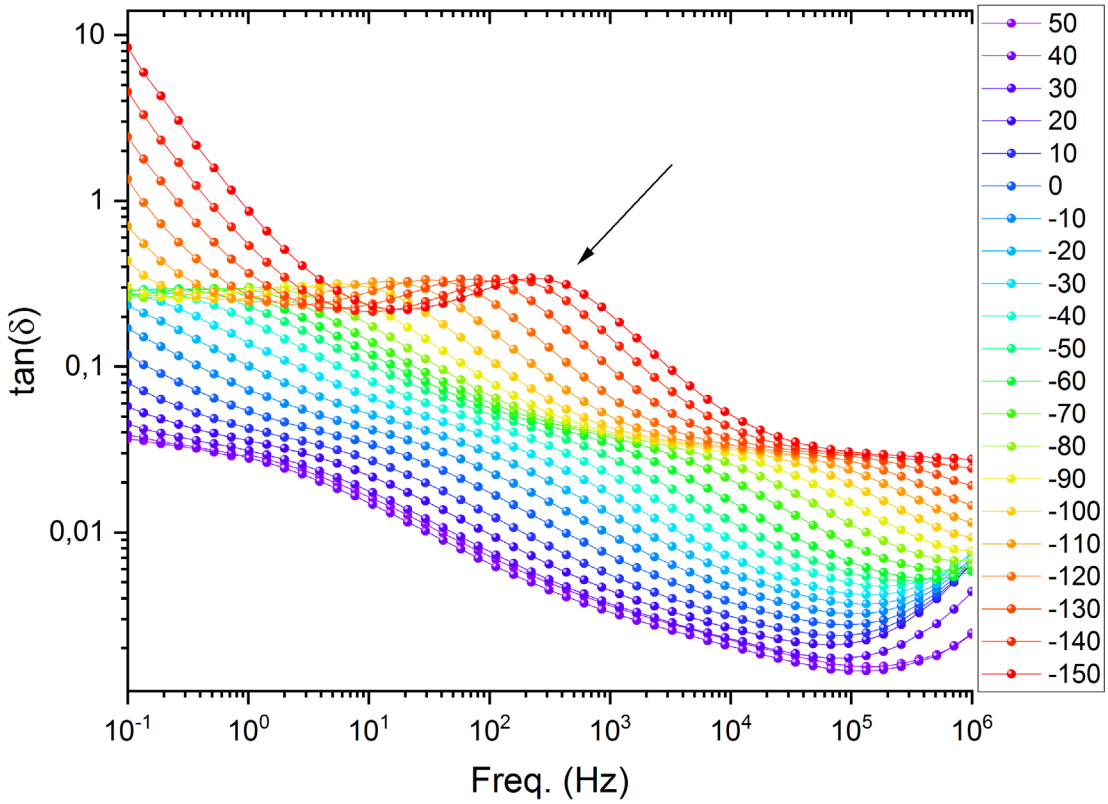

Fig. 3c. Frequency dependence of the tangent of dielectric loss tan (δ) measured at different temperatures for the PhA sensitized by the IS10 dye

to vary the properties of the composite material by adding dyes of different molecules and influence the efficiency and durability of the devices. Both dyes contribute to dielectric changes due to denser packaging of the material given the presence of dye molecules. According to the obtained data, we can conclude that the dye carrying 5-(methylene) barbituric acid in its molecule makes a greater change in the dielectric properties of the system than the dye with 2-cyanoacrylic acid as an anchor group, which indirectly implies better ability to fit into the porous titanium dioxide film, not only by physical penetration into the pores, but also chemically, more radically changing the characteristics of the composite.

Conflict of Interest

The authors declare that there is no conflict of interest, either existing or potential.

Author Contributions

Conceptualization, methodology: S. A. Kozyukhin; device fabrication: E. V. Tekshina, A. S. Steparuk, D. A. Krupanova; validation: P. I. Lazarenko; writing-original draft preparation: E. V. Tekshina, P. I. Lazarenko; supervision: S. A. Kozyukhin.

References

Berni, A., Mennig, M., Schmidt, H. (2004) Doctor Blade. In: M. A. Aegerter, M. Mennig (eds.). *Sol-Gel technologies for glass producers and users*. Boston: Springer Publ., pp. 89–92. https://doi.org/10.1007/978-0-387-88953-5_10 (In English)

Bonkerud, J., Zimmermann, C., Weiser, P. M. et al. (2021) On the permittivity of titanium dioxide. *Scientific Reports*, 11 (1), article 12443. https://doi.org/10.1038/s41598-021-92021-5 (In English)

Huang, J., Lim, P. C., Shen, L. et al. (2005) Cubic silsesquioxane-polyimide nanocomposites with improved thermomechanical and dielectric properties. *Acta Materialia*, 53 (8), 2395–2404. https://doi.org/10.1016/j.actamat.2005.02.001 (In English)

Kim, J.-H., Han, S.-H. (2020) Energy generation performance of window-type dye-sensitized solar cells by color and transmittance. *Sustainability*, 12 (21), article 8961. https://doi.org/10.3390/su12218961 (In English)

Mohamed, J. J., Hutagalung, S. D., Ain, M. F., Ahmad, Z. A. (2011) Effect of excess TiO_2 in $CaCu_3Ti_4O_{12}$ on the microstructure and dielectric properties. *Journal of Ceramic Processing Research*, 12 (5), 496–499, http://dx.doi.org/10.36410/jcpr.2011.12.5.496 (In English)

O'Regan, B., Grätzel, M. (1991) A low-cost, high-efficiency solar cell based on dye-sensitized colloidal TiO_2 films. *Nature*, 353, 737–740. https://doi.org/10.1038/353737a0 (In English)

Ramesan, M. T. (2015) Processing characteristics and mechanical and electrical properties of chlorinated styrene-butadiene rubber/fly ash composites. *Journal of Thermoplastic Composite Materials*, 28 (9), 1286–1300. https://doi.org/10.1177/0892705713505611 (In English)

Romeu, M. C., Oliveira, R. G. M., Sales, A. J. M. (2013) Impedance spectroscopy study of TiO_2 addition on the ceramic matrix $Na_2Nb_4O_{11}$. *Journal of Materials Science: Materials in Electronics*, 24 (12), 4993–4999. https://doi.org/10.1007/s10854-013-1514-6 (In English)

Steparuk, A. S., Irgashev, R. A., Zhilina, E. F. et al. (2022) Performance evaluation of dye-sensitized solar cells (DSSCs) based on metal-free thieno[3,2-b]indole dyes. *Journal of Materials Science: Materials in Electronics*, 33 (9), 6307–6317. https://doi.org/10.1007/s10854-022-07805-w (In English)

Szindler, M., Szindler, M., Drygała, A. et al. (2021) Dye-sensitized solar cell for building-integrated photovoltaic (BIPV) applications. *Materials*, 14 (3), article 3743. http://dx.doi.org/10.3390/ma14133743 (In English)

Wang, D. H., Goh, W. C., Ning, M., Ong, C. K. (2006) Effect of Ba doping on magnetic, ferroelectric, and magnetoelectric properties in mutiferroic $BiFeO_3$ at room temperature. *Applied Physics Letters*, 88 (21), article 212907. http://dx.doi.org/10.1063/1.2208266 (In English)

Wypych, A., Bobowska, I., Tracz, M. et al. (2014) Dielectric properties and characterisation of titanium dioxide obtained by different chemistry methods. *Journal of Nanomaterials*, 2014, article 124814. https://doi.org/10.1155/2014/124814 (In English)

Condensed Matter Physics.
Thermal properties of solids

UDC 538.935

EDN VRRAMV
https://www.doi.org/10.33910/2687-153X-2024-5-1-18-20

Thermoelectric energy conversion: Assessment of limiting capabilities

V. M. Grabov ✉[1], V. A. Komarov [1], V. A. Gerega [1], A. V. Suslov [1]

[1] Herzen State Pedagogical University of Russia, 48 Moika Emb., Saint Petersburg 191186, Russia

Authors

Vladimir M. Grabov, ORCID: 0000-0003-0215-6474, e-mail: vmgrabov@yandex.ru

Vladimir A. Komarov, ORCID: 0000-0002-2482-0885, e-mail: va-komar@yandex.ru

Vasilisa A. Gerega, ORCID: 0000-0003-4235-7713, e-mail: gerega.vasilisa96@gmail.com

Anton V. Suslov, ORCID: 0000-0003-1934-245X, e-mail: a.v_suslov@mail.ru

For citation: Grabov, V. M., Komarov, V. A., Gerega, V. A., Suslov, A. V. (2024) Thermoelectric energy conversion: Assessment of limiting capabilities. *Physics of Complex Systems*, 5 (1), 18–20. https://www.doi.org/10.33910/2687-153X-2024-5-1-18-20 EDN VRRAMV

Received 8 December 2023; reviewed 10 January 2024; accepted 10 January 2024.

Funding: This study was supported by the Ministry of Education of the Russian Federation as part of the state commissioned assignment (project No. VRFY-2023-0005).

Abstract. Based on a thermodynamic ratio between the thermopower coefficient and entropy of the electrically conducting medium, we obtained an estimated value of the thermoelectric efficiency parameter ZT for an electronic system of fully ionised plasma. An example of such a system, which is in the most disordered state, is the electron-nuclear plasma of the Sun. The resulting universal value $ZT = (25/6)$ can be considered as an assessment of the limiting capabilities of thermoelectric energy conversion.

Keywords: thermoelectricity, the most disordered state of an electronic system, solar plasma, dimensionless parameter of thermoelectric efficiency ZT, limit value of ZT

Introduction

As already noted (Grabov et al. 2020), thermoelectric energy converters are widely used in instrument engineering and technology, making the task of increasing the thermoelectric efficiency parameter particularly interesting. Thermoelectric efficiency is expressed as $ZT = \left(\alpha^2\sigma/\kappa\right)$, where α is the thermopower coefficient (Seebeck coefficient), σ is the conductivity coefficient, and κ is the heat conductivity coefficient (Gross 1961; Ioffe 1960). Currently, the best thermoelectric materials are characterized by the values of the dimensionless efficiency parameter $ZT \approx 1.5–1.8$ (Szczech et al. 2011). Materials demonstrating higher values of $ZT > 2.4$ have not exhibited stable reproducibility so far and still remain laboratory results with no practical applicability (D'Angelo et al. 2023). Intensive research to find ways to increase the ZT of thermoelectric materials is now underway, but there is a lack of studies investigating fundamental restrictions on a possible increase in the ZT of thermoelectric materials. We consider it possible to approach an assessment of the limiting capabilities of thermoelectric energy conversion on the basis of an analysis of thermoelectric phenomena from the standpoint of modern physical kinetics and thermodynamics (Anselm 1978; Askerov 1985; Grabov et al. 2020; Szczech et al. 2011).

On the theory of thermoelectric phenomena

The following system of equations for the density of electric charge (j_q) and heat (j_Q) fluxes is usually used as a starting point for describing thermoelectric phenomena in electrically conducting substances based on the thermodynamics of irreversible processes and physical kinetics (Anselm 1973; 1978; Askerov 1985):

$$j_q = \sigma E - \alpha\sigma \mathrm{grad} T ,$$

$$j_Q = -\kappa \mathrm{grad} T + \pi j_q . \quad (1)$$

The Thomson relation between the Peltier coefficient (π) and the Seebeck coefficient (α) follows from the symmetry condition of the Onsager kinetic coefficients, (Anselm 1973):

$$\pi = \alpha T . \quad (2)$$

Based on the thermodynamics of irreversible processes, it is shown that the thermopower coefficient α represents the entropy transferred by one charge carrier s_i, related to the value of this charge q_i. It is true for the electronic system (Anselm 1973; Grabov et al. 2020):

$$\alpha = S_i / e . \quad (3)$$

Assessment of the limiting capabilities of thermoelectric energy conversion

In its physical meaning, entropy is a measure of a system's disorder (Anselm 1973). Therefore, we can expect that the highest efficiency of thermoelectric energy conversion will correspond to an electrically conducting substance with the highest degree of disorder. From this point of view, let us consider a system of electrons in various conducting substances. Since the entropy of a system is related to its heat capacity, it is obvious that the state of the electronic system described by the Maxwell distribution (for which $C_v = (3/2)k$) is characterized by the highest entropy. In nature, a state in which the electron system is described by the Maxwell distribution is the one of a fully ionised electron-ion plasma — for example, the electron-nuclear plasma of the Sun (Kotelnikov 2013). According to (Kotelnikov 2013), in a stationary electron-ion plasma, in the presence of a temperature gradient and absence of an electric current, and as a result of the thermal diffusion of the system of electrons relative to the system of nuclei, an electric field is formed, the intensity vector $\vec{E}$ of which is determined by the following condition:

$$eE = \frac{5}{2} k \frac{dT}{dx} ,$$

$$E = \frac{5}{2} \frac{k}{e} \frac{dT}{dx} = \alpha \frac{dT}{dx} . \quad (4)$$

Thus, plasma thermopower is determined mainly by electrons, with the thermopower coefficient expressed through the ratio of ») universal constants, such as the Boltzmann constant, to the electron charge:

$$\alpha = \frac{5}{2} \frac{k}{e} . \quad (5)$$

According to (Kotelnikov 2013), thermal and electrical conductivity of a plasma is also determined by a system of electrons that complies with the Maxwell distribution. The ratio of contributions of the system of electrons and ions to transport phenomena in a fully ionised plasma is proportional to the square root of the ratio of the masses of ions and electrons $\sqrt{m_i / m_e}$ (Kotelnikov 2013). So, the contribution of ions to these phenomena can be neglected, and the problems of electronic transfer phenomena can be solved

relative to the stationary ion system (Kotelnikov 2013). In this case, as shown in the classical Drude–Lorentz theory of metals (Ashcroft, Mermin 1976), the ratio of the coefficients of thermal conductivity κ and electrical conductivity σ of the electronic system is determined by the universal Lorentz number L, also expressed through the same universal constants (5) (Ashcroft, Mermin 1976):

$$\frac{\kappa}{\sigma} = \frac{3}{2}\left(k/e\right)^2 T = LT\,,$$

$$L = \frac{3}{2}\left(k/e\right)^2\,. \tag{6}$$

For the dimensionless indicator of thermoelectric efficiency ZT of an electronic system in the most disordered state, characterized by the highest entropy, we obtain the following relation:

$$ZT = \frac{\alpha^2\sigma}{\kappa}T = \frac{\alpha^2}{L} = \frac{25}{6} \approx 4.17\,. \tag{7}$$

Thus, the ZT value, determined by expression (7) for the electronic system in the most disordered state characterised by the highest entropy, can be considered as an approximate estimate of the limiting value of the dimensionless efficiency coefficient of thermoelectric energy conversion. It is also interesting that for the extremely disordered state of the electronic system, the universal constants included in Z are reduced, which gives simply the universal number (7) for the ZT parameter: $ZT = (25/6)$. Based on the modern achievements of $ZT \approx 1.5$–1.8 (Szczech et al. 2011) and as follows from (7), developers of thermoelectric materials still have something to strive for.

Conflict of Interest

The authors declare that there is no conflict of interest, either existing or potential.

Author Contributions

Vladimir Grabov — research concept development, discussion, preparation of the manuscript, editing and supervision; Vladimir Komarov — discussion, preparation of the manuscript and editing; Vasilisa Gerega — discussion and editing; Anton Suslov — discussion and editing. All the authors have read and agreed on the published version of the manuscript.

References

Anselm, A. I. (1973) *Osnovy statisticheskoj fiziki i termodinamiki [Fundamentals of statistical physics and thermodynamics]*. Moscow: Nauka Publ., 424 p. (In Russian)

Anselm, A. I. (1978) *Vvedenie v teoriyu poluprovodnikov [Introduction to semiconductor theory]*. Moscow: Nauka Publ., 616 p. (In Russian)

Ashcroft, N., Mermin N. D. (1976) *Solid State Physics*. Philadelphia: Saunders College Publ., 833 p. (In English)

Askerov, B. M. (1985) *Elektronnye yavleniya perenosa v poluprovodnikakh [Electronic transport phenomena in semiconductors]*. Moscow: Nauka Publ., 320 p. (In Russian)

D'Angelo, M., Galassi C., Lecis N. (2023) Thermoelectric materials and applications: A review. *Energies*, 16 (17), article 6409. https://doi.org/10.3390/en16176409 (In English)

Grabov, V. M., Komarov, V. A., Demidov, E. V. (2020) Thermoelectric phenomena and thermodynamic laws. *Physics of Complex Systems*, 1 (2), 74–77. https://doi.org/10.33910/2687-153X-2020-1-2-74-77 (In English)

Gross, E. T. B. (1961) Efficiency of thermoelectric devices. *American Journal of Physics*, 29 (11), 729–731. https://doi.org/10.1119/1.1937584 (In English)

Ioffe, A. F. (1960) *Poluprovodnikovye termoelementy [Semiconductor thermoelements]*. Moscow: USSR Academy of Sciences Publ., 188 p. (In Russian)

Kotelnikov, I. A. (2013) *Lektsii po fizike plazmy [Lectures on plasma physics]*. Moscow: BINOM Publ., 384 p. (In Russian)

Szczech, J. R., Higgins, J. M., Jin, S. (2011) Enhancement of the thermoelectric properties in nanoscale and nanostructured materials. *Journal of Materials Chemistry*, 21 (12), 4037–4055. https://doi.org/10.1039/C0JM02755C (In English)

Theoretical Physics.
Physics of atoms and molecules

UDC 539.1

EDN UBYSBH
https://www.doi.org/10.33910/2687-153X-2024-5-1-21-29

The hyperbolic matrix method for wave packet treatment of atomic and molecular dynamics

M. Yu. Yakovlev ✉[1], A. K. Belyaev [1]

[1] Herzen State Pedagogical University of Russia, 48 Moika Emb., Saint Petersburg 191186, Russia

Authors

Maxim Yu. Yakovlev, ORCID: 0000-0002-1562-7370, e-mail: yakovlev.max2000@yandex.ru

Andrey K. Belyaev, ORCID: 0000-0001-8834-1456, e-mail: belyaev@herzen.spb.ru

For citation: Yakovlev, M. Yu., Belyaev, A. K. (2024) The hyperbolic matrix method for wave packet treatment of atomic and molecular dynamics. *Physics of Complex Systems*, 5 (1), 21–29. https://www.doi.org/10.33910/2687-153X-2024-5-1-21-29 EDN UBYSBH

Received 30 November 2023; reviewed 10 January 2024; accepted 10 January 2024.

Funding: The research was supported by the Russian Science Foundation (the Russian Federation), Project No. 22-23-01181.

Abstract. The hyperbolic matrix method for the treatment of atomic and molecular nuclear dynamics is derived by means of the wave packet technique within the Born–Oppenheimer approach formalism. This method allows one to calculate the evolution of a wave packet by means of the product of usual matrices instead of the time propagation of matrix exponentials. We provide a detailed description of this method, considering Tully's model as an example. We also show good agreement with the Landau–Zener model application.

Keywords: wave packet, atomic and molecular collisions, non-adiabatic transitions, nuclear dynamics, matrix exponential

Introduction

The wave packet method is an efficient method of inelastic process investigation. In this method, a wave function evolution is calculated based on a time-dependent Schrodinger equation with initial conditions for a free particle written in the form of a superposition of de Broglie waves, the so-called wave packet. It has been proven that wave packet propagation is an efficient technique for investigating nuclear dynamics in atomic and molecular collisions. There are many investigations of wave packet application for nuclear and molecular collisions: see, for example, (Akpinar, Surucu 2011; Mao et al. 2022; Tully 1990; Vaeck, et al. 1998) and references therein. Time propagation of a wave packet can be calculated by different means: see, e. g., (Balakrishnan et al. 1997). One of them is propagation by an evolution operator and the split-operator method. This approach leads to matrix exponentials, which are a challenge for numerical calculations. Thus, we describe a new method for accomplishing time–evolution calculations without matrix exponentials.

Method

The main equations

The most widely used approach for treating inelastic atomic and molecular collisions, the Born–Oppenheimer approach, splits the total Hamiltonian of a molecule, as well as a collision into two parts: the kinetic energy operator of nucleus motion $\hat{T}_N$ and the electronic Hamiltonian $\hat{H}_e$:

$$\hat{H} = \hat{H}_e + \hat{T}_N \ . \tag{1}$$

In this case, the total wave function $\psi(\vec{R},\vec{r},t)$ of a quasi-molecule can be derived from the time-dependent Schrodinger equation:

$$i\hbar\frac{\partial}{\partial t}\psi(\vec{R},\vec{r},t) = (\hat{H}_e + \hat{T}_N)\psi(\vec{R},\vec{r},t) \ , \tag{2}$$

$\vec{R}$ being the internuclear vector and $\vec{r}$, the electronic coordinates. The wave function $\psi(\vec{R},\vec{r},t)$ can be written as a sum of partial wave functions:

$$\psi(\vec{R},\vec{r},t) = \sum_{J,M_J}\psi_{J,M_J}(\vec{R},\vec{r},t) \ , \tag{3}$$

where J is the quantum number of the total angular momentum of a molecule, and M_J is the quantum number of the projection of the total angular momentum onto the internuclear axis. Each partial wave function satisfies the Schrodinger equation (2). By expanding a partial wave function on the basis of diabatic electronic wave functions $\varphi_j^{di}(\vec{r};R)$, one gets:

$$\psi_{J,M_J}(\vec{R},\vec{r},t) = \sum_j \chi_j(\vec{R},t)\varphi_j^{di}(\vec{r};R) \ , \tag{4}$$

where $\chi_j(\vec{R},t)$ is the nuclear wave function.

The nuclear wave function in Eq. (4) depends on molecule symmetry properties. Let us consider a case of the Σ symmetry. A nuclear wave function can be written as

$$\chi_j(\vec{R},t) = \frac{F_j(R,t)}{R}Y_{J,M_J}(\theta,\varphi) \ , \tag{5}$$

where $F_j(R,t)$ is the radial nuclear wave function and $Y_{J,M_j}(\theta,\varphi)$, the spherical nuclear wave function. Then the partial wave function reads:

$$\psi_{J,M_J}(\vec{R},\vec{r},t) = \sum_j \frac{F_j(R,t)}{R}Y_{J,M_J}(\theta,\varphi)\varphi_j^{di}(\vec{r};R) \ . \tag{6}$$

By substituting the partial wave function into Eq. (2), multiplying by a complex conjugate wave function $\left(\varphi_k^{di}(\vec{r};R)\right)^*$ and integrating over the electronic coordinates, one obtains a system of differential equations:

$$i\hbar\frac{\partial F_k(R,t)}{\partial t} = \left(-\frac{\hbar^2}{2\mu}\frac{\partial^2}{\partial R^2} + \frac{\hbar^2}{2\mu}\frac{J(J+1)}{R^2} + H_{kk}\right)F_k(R,t) + \sum_{j\neq k}F_j(R,t)H_{kj} \ , \tag{7}$$

where $H_{kj} = \langle\varphi_k^{di}(\vec{r};R)|\hat{H}_e|\varphi_j^{di}(\vec{r};R)\rangle$ is an element of the Hamiltonian matrix and μ is a reduced mass.

 https://www.doi.org/10.33910/2687-153X-2024-5-1-21-29

Let us write the system of differential equations (7) in the matrix form:

$$\dot{\boldsymbol{F}} = (\boldsymbol{T} + \boldsymbol{H})\boldsymbol{F} \tag{8}$$

where $\dot{\boldsymbol{F}} = (\partial F_1(R,t)/\partial t, \dots, \partial F_n(R,t)/\partial t)^T$, $\boldsymbol{F} = \left(F_1(R,t), \dots, F_n(R,t)\right)^T$,

$$[\boldsymbol{T}]_{kj} = \left(-\frac{i}{\hbar}\frac{\hbar^2\hat{k}^2}{2\mu}\right)\delta_{kj}, \qquad [\boldsymbol{H}]_{kj} = -\frac{i}{\hbar}\left(\frac{\hbar^2}{2\mu}\frac{J(J+1)}{R^2}\right)\delta_{kj} - \frac{i}{\hbar}H_{kj}\,. \tag{9}$$

The solution can be written as a matrix exponential:

$$\boldsymbol{F} = e^{(\boldsymbol{T}+\boldsymbol{H})t}\boldsymbol{F_0}\,, \tag{10}$$

$\boldsymbol{F_0} = \left(F_1(R,0), \dots, F_n(R,0)\right)^T$ being the vector of initial functions.

The main problem is in the calculation of a derivative of $\hat{k}$ in the matrix exponent. The point is that the matrix exponential of a sum of two matrices is not equal to a product of two matrix exponentials because the matrices do not commute. The split-operator method (Balakrishnan et al. 1997) solves this by splitting the matrix exponential into three terms:

$$e^{(\boldsymbol{T}+\boldsymbol{H})t} = e^{\frac{\boldsymbol{H}}{2}t}e^{\boldsymbol{T}t}e^{\frac{\boldsymbol{H}}{2}t} + O(t^3) \approx e^{\frac{\boldsymbol{H}}{2}t}e^{\boldsymbol{T}t}e^{\frac{\boldsymbol{H}}{2}t}\,. \tag{11}$$

Thus, one can multiply the function on each matrix exponential one by one in the coordinate and momentum spaces. It allows one to treat $\hat{k}$ as a number, not as a derivative. Finally, the algorithm is the following:

1. $\boldsymbol{G}^{st.1} = e^{\frac{\boldsymbol{H}}{2}t}\boldsymbol{F_0}$;
2. $\boldsymbol{D}^{st.2} = FT[\boldsymbol{G}^{st.1}]$;
3. $\boldsymbol{D}^{st.3} = e^{\boldsymbol{T}t}\boldsymbol{D}^{st.2}$;
4. $\boldsymbol{G}^{st.4} = IFT[\boldsymbol{D}^{st.3}]$;
5. $\boldsymbol{F} = e^{\frac{\boldsymbol{H}}{2}t}\boldsymbol{G}^{st.4}$,

where $\boldsymbol{G}^{st.N}$ is the vector of the N-step wave function in the coordinate space, $\boldsymbol{D}^{st.N}$ is the vector of the N-step wave function in the momentum space; FT is the Fourier transform and IFT is the inverse Fourier transform. For numerical calculations, the Fast Fourier transform algorithm can be used.

The initial condition is set up as follows. The wave function of the initial state can be chosen in the form of a wave packet:

$$W(R,0) = \left(\frac{1}{a\sqrt{\pi}}\right)^{1/2} e^{-\frac{1}{2}\left(\frac{R-R_0}{a}\right)^2 + ik_0R}\,, \tag{12}$$

where a is the coefficient of the wave packet width, R_0, the center of the wave packet and k_0, the average momentum of the wave packet.

The hyperbolic matrix method

In practice, there is a problem of getting a matrix exponential. There are different methods and algorithms for this: The Taylor approximation, the Pade approximation, the scaling and squaring method (Al-Mohy, Higham 2010; 2011), etc. It is also possible to use the hyperbolic matrix method.

The method is based on the expansion of a matrix exponential by Taylor series and is valid for symmetric matrices. Off-diagonal Hamiltonian diabatic matrix elements should be equal for this method.

Let us consider the case of the matrix (2 × 2) :

$$\boldsymbol{A} = \begin{pmatrix} a & c \\ c & b \end{pmatrix}, \tag{13}$$

the matrix exponential $e^{\boldsymbol{A}}$ is defined as:

$$e^{\boldsymbol{A}} = \sum_{k=0}^{\infty} \frac{1}{k!} \boldsymbol{A}^k . \tag{14}$$

The matrix exponential $e^{\boldsymbol{A}}$ can be accepted as a multiplication of three matrix exponentials using a method similar to the split-operator method and with the same precision:

$$e^{\boldsymbol{A}} \approx e^{\frac{\boldsymbol{C}}{2}} e^{\boldsymbol{B}} e^{\frac{\boldsymbol{C}}{2}}, \tag{15}$$

where

$$\frac{\boldsymbol{C}}{2} = \begin{pmatrix} 0 & \frac{c}{2} \\ \frac{c}{2} & 0 \end{pmatrix}, \tag{16}$$

$$\boldsymbol{B} = \begin{pmatrix} a & 0 \\ 0 & b \end{pmatrix}. \tag{17}$$

Then the matrix exponentials $e^{\boldsymbol{B}}$ and $e^{\frac{\boldsymbol{C}}{2}}$ read:

$$e^{\boldsymbol{B}} = \sum_{k=0}^{\infty} \frac{1}{k!} \begin{pmatrix} a & 0 \\ 0 & b \end{pmatrix}^k, \tag{18}$$

$$e^{\frac{\boldsymbol{C}}{2}} = \sum_{k=0}^{\infty} \frac{1}{k!} \begin{pmatrix} 0 & \frac{c}{2} \\ \frac{c}{2} & 0 \end{pmatrix}^k . \tag{19}$$

There is the following rule for raising matrices to powers:

$$\begin{pmatrix} a & 0 \\ 0 & b \end{pmatrix}^k = \begin{pmatrix} a^k & 0 \\ 0 & b^k \end{pmatrix} \tag{20}$$

and

$$\begin{pmatrix} 0 & \frac{c}{2} \\ \frac{c}{2} & 0 \end{pmatrix}^k = \begin{cases} \begin{pmatrix} \left(\frac{c}{2}\right)^k & 0 \\ 0 & \left(\frac{c}{2}\right)^k \end{pmatrix}, & k = 2n, \ \ n \in \mathbb{N}; \\ \begin{pmatrix} 0 & \left(\frac{c}{2}\right)^k \\ \left(\frac{c}{2}\right)^k & 0 \end{pmatrix}, & k = 2n+1, \ \ n \in \mathbb{N}. \end{cases} \tag{21}$$

Thus, for $e^{\boldsymbol{B}}$ we have the following:

$$e^{\boldsymbol{B}} = \begin{pmatrix} \sum_{k=0}^{\infty} \frac{1}{k!} a^k & 0 \\ 0 & \sum_{k=0}^{\infty} \frac{1}{k!} b^k \end{pmatrix} = \begin{pmatrix} e^a & 0 \\ 0 & e^b \end{pmatrix}, \tag{22}$$

 https://www.doi.org/10.33910/2687-153X-2024-5-1-21-29

and for $e^{\frac{c}{2}}$ the matrix reads:

$$e^{\frac{c}{2}} = \begin{pmatrix} \sum_{k=0}^{\infty} \frac{1}{2k!}\left(\frac{c}{2}\right)^{2k} & \sum_{k=0}^{\infty} \frac{1}{(2k+1)!}\left(\frac{c}{2}\right)^{2k+1} \\ \sum_{k=0}^{\infty} \frac{1}{(2k+1)!}\left(\frac{c}{2}\right)^{2k+1} & \sum_{k=0}^{\infty} \frac{1}{2k!}\left(\frac{c}{2}\right)^{2k} \end{pmatrix}, \tag{23}$$

$$e^{\frac{c}{2}} = \begin{pmatrix} cosh\left(\frac{c}{2}\right) & sinh\left(\frac{c}{2}\right) \\ sinh\left(\frac{c}{2}\right) & cosh\left(\frac{c}{2}\right) \end{pmatrix}. \tag{24}$$

This method allows one to move from the matrix exponential to a usual matrix. This finding is strict because the Taylor series are exact.

Thus, returning to the solution (10), one can see that the matrix exponential should be split into the following three matrix exponentials:

$$e^{(\boldsymbol{T}+\boldsymbol{H})t} = e^{\frac{\boldsymbol{H_{od}}}{2}t} e^{(\boldsymbol{T}+\boldsymbol{U})t} e^{\frac{\boldsymbol{H_{od}}}{2}t} + O(t^3) \approx e^{\frac{\boldsymbol{H_{od}}}{2}t} e^{(\boldsymbol{T}+\boldsymbol{U})t} e^{\frac{\boldsymbol{H_{od}}}{2}t} \tag{25}$$

where

$$[\boldsymbol{H_{od}}]_{kj} = -\frac{i}{\hbar} H_{kj}(1-\delta_{kj}), \tag{26}$$

$$[\boldsymbol{U}]_{kj} = -\frac{i}{\hbar}\left(\frac{\hbar^2}{2\mu}\frac{J(J+1)}{R^2} + H_{kj}\right)\delta_{kj}, \qquad [\boldsymbol{T}]_{kj} = \left(-\frac{i}{\hbar}\frac{\hbar^2\hat{k}^2}{2\mu}\right)\delta_{kj}. \tag{27}$$

Then the split-operator method can be applied to the central matrix exponential of Eq. (25):

$$e^{(\boldsymbol{T}+\boldsymbol{H})t} \approx e^{\frac{\boldsymbol{H_{od}}}{2}t} e^{\frac{\boldsymbol{U}}{2}t} e^{\boldsymbol{T}t} e^{\frac{\boldsymbol{U}}{2}t} e^{\frac{\boldsymbol{H_{od}}}{2}t}. \tag{28}$$

Using the hyperbolic matrix method for external matrix exponentials and taking into account that $H_{12} = H_{21}$, we get:

$$e^{(\boldsymbol{T}+\boldsymbol{H})t} = \boldsymbol{H_y U_e T_e U_e H_y}, \tag{29}$$

where

$$[\boldsymbol{U_e}]_{kj} = \exp\left(-\frac{1}{2}\frac{i}{\hbar}t\left(\frac{\hbar^2}{2\mu}\frac{J(J+1)}{R^2} + H_{kj}\right)\right)\delta_{kj}, \tag{30}$$

$$[\boldsymbol{T_e}]_{kj} = \exp\left(\left(-\frac{i}{\hbar}t\frac{\hbar^2\hat{k}^2}{2\mu}\right)\right)\delta_{kj}, \tag{31}$$

$$\left[\boldsymbol{H_y}\right]_{kj} = \begin{cases} cosh\left(-\frac{i}{\hbar}t\frac{H_{12}}{2}\right), & k = j; \\ sinh\left(-\frac{i}{\hbar}t\frac{H_{12}}{2}\right), & k \neq j. \end{cases} \tag{32}$$

Finally, the solution (10) can be written as:

$$\boldsymbol{F} = \boldsymbol{H_y U_e T_e U_e H_y F_0}. \tag{33}$$

Thus, we found that the final solution, which was initially expressed via the matrix exponential, see Eq. (10), can be calculated as a product of the number of usual matrices without any matrix exponential, see Eq. (33).

Extension and generalization of the hyperbolic matrix method

Simplicity of the hyperbolic matrix method is marred by the heavy calculations it requires. The key point of the matrix exponential method is to express $e^{\boldsymbol{A}}$, $\boldsymbol{A}$ being a symmetric $(N \times N)$ matrix, via a multiplication of $2C_N^2 + 1$ matrices, where C_n^k is the combination number.

Assume $\boldsymbol{A}$ contains $a_{jk} = a_{kj}$, then

$$e^{\boldsymbol{A}} = \left(\prod_{m=1}^{N-1}\prod_{n>m}^{N}(\boldsymbol{I} + \boldsymbol{C^{mn}})\right)\boldsymbol{B}\left(\prod_{m=N-1}^{1}\prod_{n>m}^{N}(\boldsymbol{I} + \boldsymbol{C^{mn}})\right), \tag{34}$$

where $\boldsymbol{I}$ is the identity matrix, and

$$[\boldsymbol{C^{mn}}]_{jk} = \left(\delta_{jm}\delta_{kn} + \delta_{km}\delta_{jn}\right)\sinh\left(\frac{a_{mn}}{2}\right) + \delta_{jk}\left(\delta_{jn} + \delta_{jm}\right)\left(\cosh\left(\frac{a_{mn}}{2}\right) - 1\right), \tag{35}$$

$$[\boldsymbol{B}]_{jk} = \delta_{jk}e^{a_{jk}}. \tag{36}$$

The formula (34) is obtained by repeating the split-operator method C_N^2 times.

Application example

Tully's model (Tully 1990) is an analytic two diabatic-state model with a non-adiabatic region. The model can be used to demonstrate a possible application of the wave packet method for investigating an inelastic collision process. Tully's article contains three different models: with a single non-adiabatic region; with a pair of adiabatic regions; and with an extended coupling with reflection. We performed a test calculation for the first model with a single adiabatic region (fig. 1).

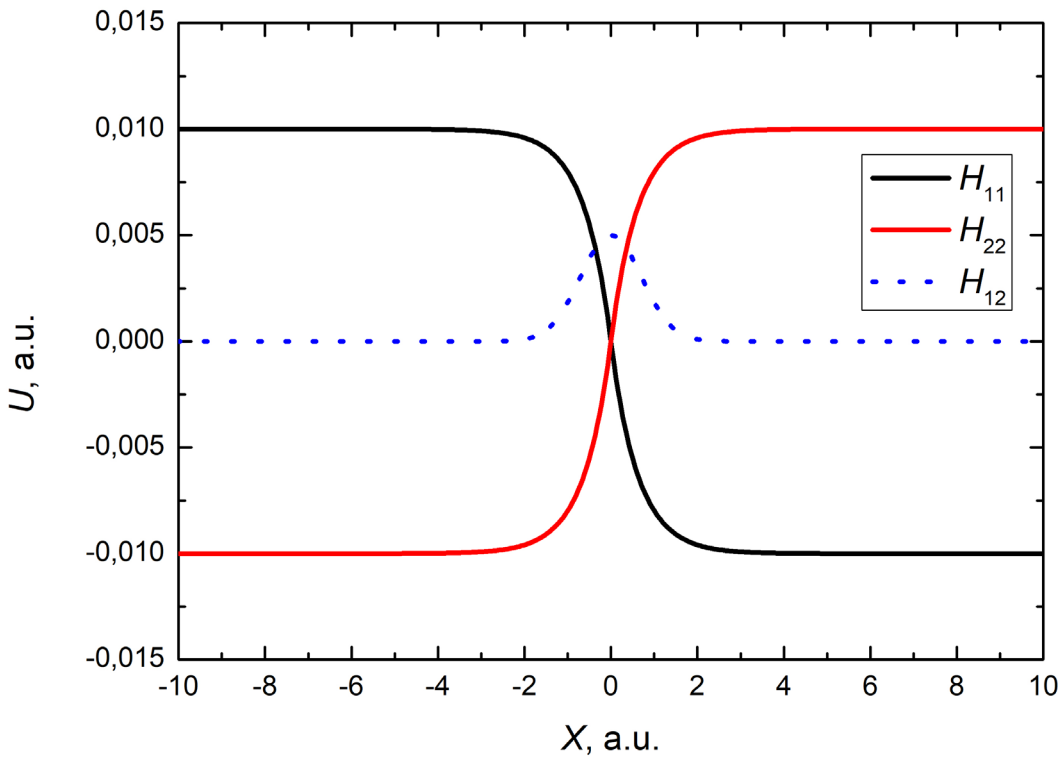

Fig. 1. Diabatic potentials and off-diagonal Hamiltonian matrix element as a function of the scattering coordinate. The solid black line is the first potential, the solid red line is the second potential, and the dotted blue line is the off-diagonal Hamiltonian matrix element

https://www.doi.org/10.33910/2687-153X-2024-5-1-21-29

The potentials and off-diagonal Hamiltonian matrix element are determined as

$$H_{11} = \begin{cases} A(1 - e^{-Bx}), & x > 0; \\ -A(1 - e^{Bx}), & x < 0, \end{cases} \tag{37}$$

$$H_{22} = -H_{11}, \tag{38}$$

$$H_{12} = H_{21} = Ce^{-Dx^2}, \tag{39}$$

where A, B, C and D are some parameters and x is the coordinate used in the model. The diabatic higher asymptotic state was chosen as the initial channel. We used the following values for the above parameters: A = 0.01, B = 1.6, C = 0.005 and D = 1.

The initial wave function was taken as a wave packet (12) with the following parameters: $a = 20/k_0$ and m = 2000. The case was investigated for a range of 3.0 a.u. ≤ k ≤ 50 a.u. that corresponds to a collision energy of 0.00225 a.u. ≤ E_{col} ≤ 0.625 a.u or 0.0612 eV ≤ E_{col} ≤ 17 eV.

The hyperbolic matrix method was used for wave packet propagation. Probability was calculated by the reactive flux method (Balakrishnan et al. 1997; Neuhauser et al. 1991), which allows one to analyze the outgoing flux of the wave packet towards the asymptotic channel, where the flux is equal to

$$j(\tilde{x}, t) = \frac{\hbar}{m} \mathrm{Im} \left(F^*(x, t) \frac{\partial F(x, t)}{\partial x} \right)_{x=\tilde{x}}, \tag{40}$$

then

$$P = \int_0^\infty j(\tilde{x}, t) dt \ . \tag{41}$$

The main advantage of flux methods is that in order to calculate the outgoing flux, the wave function should be known only at one point $\tilde{x}$. The method provides nonadiabatic transition probability as a function of the average wave packet momentum k_0.

The results of the wave packet calculations of the nonadiabatic transition probabilities have been compared with the probabilities calculated by the Landau–Zener model:

$$P_{12} \approx e^{-\frac{2\pi H_{12}^2}{\left(\frac{dH_{11}}{dx} - \frac{dH_{22}}{dx}\right)v}}, \tag{42}$$

where $v = \frac{\hbar k_0}{m}$. The Landau–Zener probability is calculated at the point $\tilde{x} = 0$, which gives the following expression according to Eqs. (37)–(39):

$$P_{12} = e^{-\frac{\pi C^2}{ABv}}. \tag{43}$$

Note that probability does not depend on the parameter D, see Eq. (39). The comparison of the calculated probabilities is presented in Fig. 2.

As follows from this figure, the results for Tully's model agree well with each other, which proves the reliability and efficiency of the hyperbolic matrix method for wave packet propagation.

Conclusions

In conclusion, an inelastic collision can be treated by the time-dependent Schrodinger equation, which can be resolved by means of a matrix exponential. The hyperbolic matrix method is a way to solve the Schrodinger equation by transforming the matrix exponential into a usual matrix. This allows one to avoid calculating matrix exponentials. The simplicity of computing a usual matrix instead of a matrix exponential is one of the advantages of the method. Its disadvantage is a rapid increase in the number of matrix multiplications with an increase in the matrix dimension leading to heavy calculations. Thus, the hyperbolic matrix method works well for low-dimensional systems. An application example for

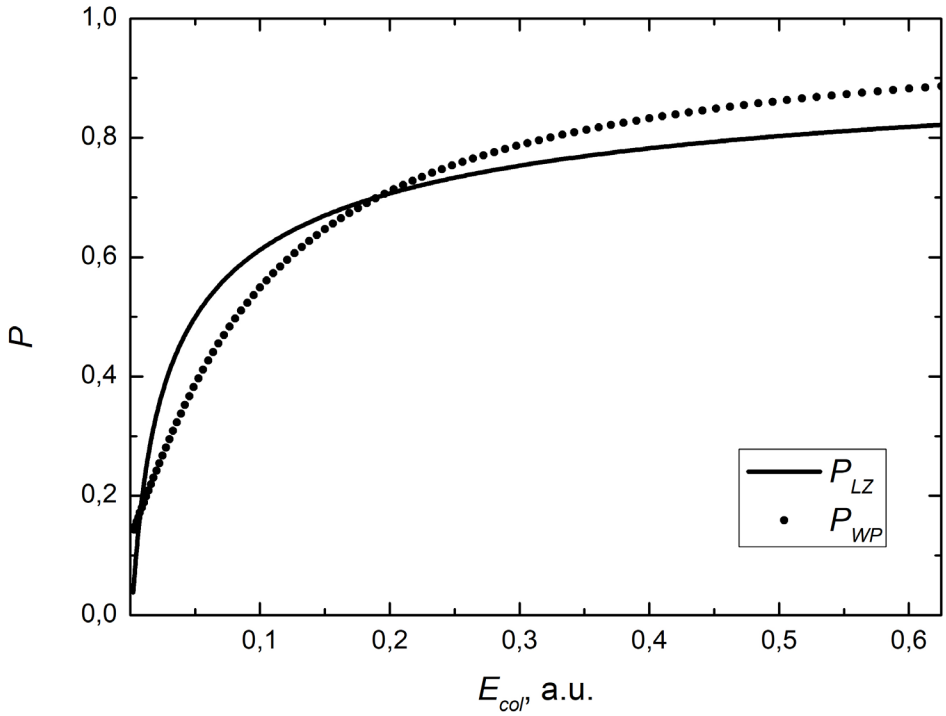

Fig. 2. Probabilities for transitions from higher to low diabatic states. The solid line represents the Landau–Zener probability while the circle symbols stand the wave-packet probabilities

Tully's model shows the method provides a good agreement with results of Landau-Zener model applications, and finally, applicability of the hyperbolic matrix method to other collision systems. In addition, it is worth emphasizing that the hyperbolic matrix method can be employed in other problems where matrix exponentials are used.

Conflict of Interest

The authors declare that there is no conflict of interest, either existing or potential.

Author Contributions

The authors have made an equal contribution to the paper.

Acknowledgements

The authors are grateful to Dr. A. S. Tiukanov for fruitful discussions.

References

Akpinar, S., Surucu, S. (2011) Time dependent wave packet study of the H-+ H2 nonreactive scattering. *Journal of Quantum Information Science*, 1 (2), 96–103. https://doi.org/10.4236/jqis.2011.12013 (In English)

Al-Mohy, A. H., Higham, N. J. (2010) A new scaling and squaring algorithm for the matrix exponential. *SIAM Journal on Matrix Analysis and Applications*, 31 (3), 970–989. https://doi.org/10.1137/09074721X (In English)

Al-Mohy, A. H., Higham, N. J. (2011) Computing the action of the matrix exponential, with an application to exponential integrators. *SIAM Journal on Scientific Computing*, 33 (2), 488–511. https://doi.org/10.1137/100788860 (In English)

Balakrishnan, N., Kalyanaraman, C., Sathyamurthy, N. (1997) Time-dependent quantum mechanical approach to reactive scattering and related processes. *Physics Reports*, 280 (2), 79–144. https://doi.org/10.1016/S0370-1573(96)00025-7 (In English)

Mao, Y., Buren, B., Yang, Z. , Chen, M. (2022) Time-dependent wave packet dynamics study of the resonances in the H + LiH^+ (v = 0, j = 0) → Li^+ + H_2 reaction at low collision energies. *Physical Chemistry Chemical Physics*, 24 (25), 15532–15539. https://doi.org/10.1039/D1CP05601H (In English)

Neuhauser, D., Baer, M., Judson, R. S., Kouri, D. J. (1991) The application of time-dependent wavepacket methods to reactive scattering. *Computer Physics Communications*, 63 (1–3), 460–481. https://doi.org/10.1016/0010-4655(91)90270-U (In English)

Tully, J. C. (1990) Molecular dynamics with electronic transitions. *The Journal of Chemical Physics*, 93 (2), 1061–1071. https://doi.org/10.1063/1.459170 (In English)

Vaeck, N., Desouter-Lecomte, M., Liévin, J. (1998) Non-adiabatic wave packet dynamics for charge exchange processes: Application to C^{4+} + H. *Journal of Physics B: Atomic, Molecular and Optical Physics*, 32 (2), 409–428. https://doi.org/10.1088/0953-4075/32/2/021 (In English)

Physics of Semiconductors. Computational materials science

UDC 538.913

EDN SUQFNX
https://www.doi.org/10.33910/2687-153X-2024-5-1-30-38

Uniaxial pressure modulation of two-dimensional materials: Insights into the structure and electronic properties of $MoTe_2$ and Sb_2Te_3

R. S. Stepanov ✉ [1]

[1] Herzen State Pedagogical University of Russia, 48 Moika Emb., Saint Petersburg 191186, Russia

Author

Roman S. Stepanov, ORCID: 0000-0003-2559-7598, e-mail: stepanovroman@herzen.spb.ru

For citation: Stepanov, R. S. (2024) Uniaxial pressure modulation of two-dimensional materials: Insights into the structure and electronic properties of $MoTe_2$ and Sb_2Te_3. *Physics of Complex Systems*, 5 (1), 30–38. https://www.doi.org/10.33910/2687-153X-2024-5-1-30-38 EDN SUQFNX

Received 16 January 2024; reviewed 6 February 2024; accepted 6 February 2024.

Funding: The research was supported by the Ministry of Education of the Russian Federation as part of the state-commissioned assignment project No. VRFY-2023-0005.

Abstract. This research focuses on DFT modeling of the effects of uniaxial pressure on the electronic and structural properties of two-dimensional materials, such as $MoTe_2$ and Sb_2Te_3. Special attention is given to the reconfiguration of the van der Waals (vdW) gap. Intuitively, the application of uniaxial pressure is expected to reduce the distance between layers, leading to a transition from 2D to 3D. Investigations under uniaxial pressure on Sb_2Te_3 revealed metallization at 3 GPa. Further pressure increase induces a phase transition at 7 GPa, resulting in the disappearance of the vdW gap in the new phase. However, a transition to a bulk phase does not always occur. In the case of $MoTe_2$, pressure leads to an isostructural transition to a metallic state at 10 GPa. A further increase in pressure to 37 GPa causes a phase transition to a two-dimensional structure with a change in the orientation of the vdW gap. It is crucial to note that this $MoTe_2$ case is analogous to the situation observed in GaSe after relaxation, which is also the subject of the study.

Keywords: 2D semiconductors, van der Waals interaction, DFT, uniaxial pressure, $MoTe_2$, Sb_2Te_3, structural transitions

Introduction

Among various techniques of manipulating quantum mechanical effects in materials, strain engineering has emerged as a powerful and versatile tool. In this field, layered materials, characterized by covalently bonded layers held together by weak van der Waals (vdW) forces, have become particularly promising. Applications vary from microchip production (Benck et al. 2014; Gao et al. 2013; Li et al. 2019; Pan et al. 2019; Wang et al. 2014) to supercapacitors and phase-change memory devices (Lee et al. 2020; Mu et al. 2021; Peng et al. 2014; Pumera et al. 2014; Raty, Noé 2020; Wang et al. 2014). The discovery of topological materials (Bernevig et al. 2006; Chen et al. 2009; Kane, Mele 2005a; Konig et al. 2007) with their unique properties has further expanded the horizons of materials science, particularly in the field of straintronics. Topological materials have attracted considerable attention due to their distinctive features. For instance, the inversion of the band gap at an odd number of time-reversed points in the Brillouin zone (Bernevig 2013; Kane, Mele 2005b; Qi, Zhang 2011) leads to interesting properties such as locking the spin momentum of surface states (Singh, Prasad 2016) and the magnetoelectric effect (Tominaga et al. 2015).

In dichalcogenides, monochalcogenides, and certain topological insulators (such as Sb_2Te_3), fine-tuning the properties by altering the interlayer distance appears feasible, due to the strong dependence of the electronic and optical properties on the width of the vdW gap (Fan et al. 2015; Stepanov et al. 2023b; Zhao et al. 2015). As the vdW gap width decreases, a transition from a layered material to a bulk one is expected, leading to radical changes in properties related to structure and non-covalent interactions. However, the anticipated transition from quasi-2D to 3D may not occur (Stepanov et al. 2023a). Therefore, it is crucial to elucidate how noncovalent interactions are distributed during the disruption of the vdW gap and how it affects the geometry and properties of the new phase.

Due to the small band gap in Sb_2Te_3 and $MoTe_2$, metallization is expected to occur before the structural phase transition. Indeed, for both Sb_2Te_3 and $MoTe_2$, external hydrostatic pressure can lead to isostructural phase transitions (IPT), often resulting in anomalies in mechanical, electrical, thermodynamic, and vibrational properties (Bera et al. 2020; Zhao et al. 2015). In this context, interlayer interaction plays a pivotal role; it has been reported that neglecting vdW may lead to the erroneous conclusion that no IPT occurs in the material (Gomis et al. 2011; Zhao et al. 2015). Studying the influence of uniaxial pressure can contribute to a better understanding of the role of vdW interaction in this process.

In this study, in order to generalize and identify patterns in the transformation of non-covalent interactions in layered materials under uniaxial compression, we examine the structure and properties of the representatives of the most promising layered materials ($MoTe_2$ dichalcogenides and Sb_2Te_3 topological insulators). Another important aspect of the study is to consider the influence of non-covalent interactions on the structure after the phase transition and how it affects the IPT.

Computational details

Calculations were performed using the CASTEP quantum chemistry package (Clark et al. 2005). The generalized gradient approximation (GGA) with the Perdew-Burke-Ernzerhof (PBE) parameterization (Ernzerhof, Scuseria 1999) with vdW corrections, important for describing interaction between the layers, was used. The vdW interactions were taken into account using the Grimme method (Grimme 2006; Grimme et al. 2010; 2011). The k space integrals and plane wave basis sets were chosen to ensure total energy convergence at 1 meV/atom. It was found that a kinetic energy cut-off of 500 eV is sufficient for all calculations. Two-Point Steepest Descent (TPSD) algorithm was chosen for the optimization in CASTEP. Such algorithm had previously (Barzilai, Borwein 1988) showed computational structures in best agreement with experimental ones, especially with the application of pressure. Pressure modeling was carried out using uniaxial pressure along the c axis of conventional cells. To carry out relaxation, the structures were optimized at a pressure of 0 GPa.

To study the bonds in phases under pressure, the electron density difference analysis (CDD) was used. For a more detailed study of the vdW interaction, the CRITIC2 code was used (Otero-de-la-Roza et al. 2009; 2014), in which the analysis of the electron density gradient (RDG) between molecular fragments (Johnson et al. 2010) was used to assess their strength.

Results

For the first investigated material, $MoTe_2$ (Fig. 1 (a, b)), as the applied uniaxial pressure increases up to 37 GPa, the valence angle decreases, but the overall structure remains unchanged. However, at a pressure of 37 GPa, a significant transformation occurs as the vdW gap collapses due to the formation of metal-chalcogen bonds through the gap. Simultaneously, based on the CDD analysis, it is observed that covalent bonds perpendicular to the Z axis are disrupted, leading to the rotation of the vdW gap and its reorientation along the Z axis (refer to Fig. 1 (c, d)). It is noteworthy that during this rearrangement, both molybdenum and tellurium maintain coordination consistent with the original structure, albeit violating the octet rule. With an even greater increase in pressure, a lateral displacement of the layers relative to each other occurs. A similar result was also observed for PbS_2 in (Lei et al. 2020).

Fig. 2 illustrates the band structures of $MoTe_2$ under varying pressures. Initially, under uniaxial pressure, the band gap is an indirect gap between the maximum of the valence band (VB) at point Γ and the minimum of the conduction band (CB), located between G- and K-points (Fig. 2 (c)). Upon closer examination, it becomes apparent that the band gap gradually decreases and approaches zero with increasing pressure, attributed to a reduction in the interlayer distance. Band overlap starts at 10 GPa between the top of the valence band and the bottom of the CB (Fig. 2 (e)). Our calculations align with experimental

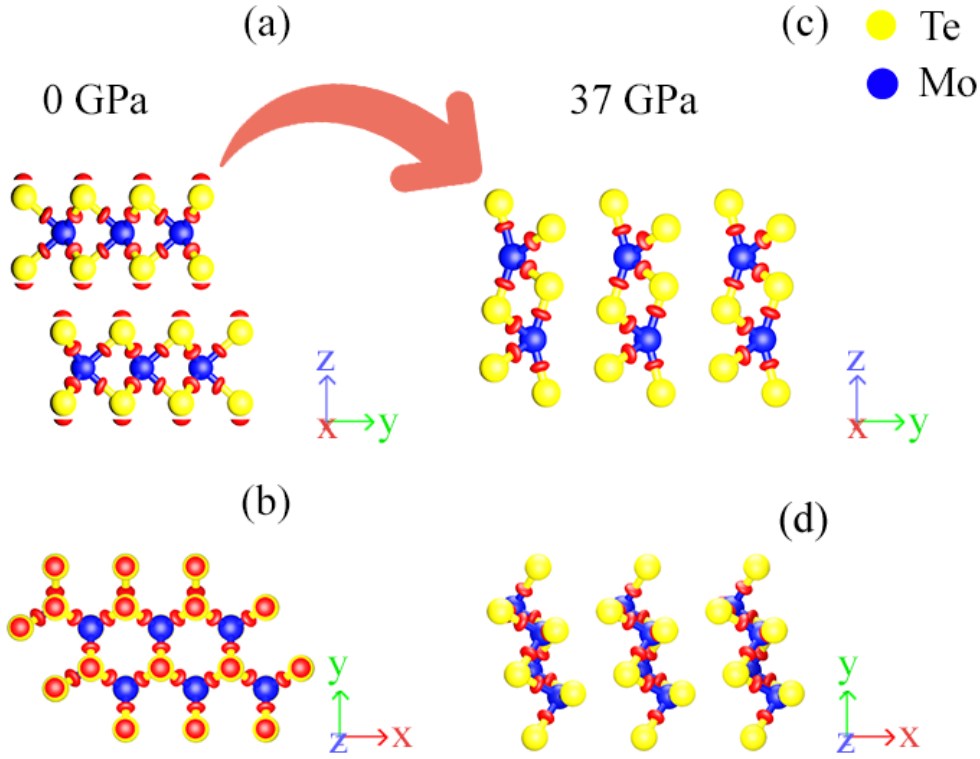

Fig. 1. Transformation of the $MoTe_2$ structure under the influence of axial pressure: (a)–(b) Initial structure (side and top view respectively), (c)–(d) New phase at 37 GPa (side and top view respectively)

measurements, where the onset of metallization occurs at a hydrostatic pressure of 9.6 GPa (Zhao et al. 2019).

With pressure increase, both the CB and VB experience energy shifts due to enhanced interlayer electronic coupling. At a pressure of 20 GPa (Fig. 2 (f)), the CB minimum and VB maximum intersect the Fermi level, signifying metallization. Importantly, the cell symmetry remains unchanged, indicating an IPT. Similar to other TMDs, pressure-induced shifts of extremes generate a series of electron and hole pockets. Given the larger atomic radius of Te and wider electron orbitals compared to Se and S, this may contribute to $MoTe_2$ achieving metallization at a lower pressure than most other TMDs such as MoS_2, $MoSe_2$, and WS_2.

As already mentioned, under pressure, the $MoTe_2$ structure does not change coordination when transitioning to a new phase and it may resemble the relaxed GaSe structure. In our previous work (Stepanov et al. 2023a), it was established that in monochalcogenides the vdW gap closes under the action of applied uniaxial pressure. Analysis of the CDD distribution revealed the formation of quasi-one-dimensional chains with non-covalent interactions between them. In this work, during the relaxation of the structure in Fig. 3 (b), it is found that the original 0 GPa phase in Fig. 3 (a) is not restored. Instead, a distortion of the 14 GPa phase occurs, which leads to a transition from chains with non-covalent interactions between them to a two-dimensional structure, albeit with an orthogonally reoriented vdW gap (Fig. 3 (c)). It is important to note that the atomic coordination returns to its original state, breaking the octet rule. Thus, both $MoTe_2$ and GaSe have in common the fact that in these materials it is possible to achieve reorientation of the vdW gap while maintaining coordination.

RDG analysis was used to confirm vdW gap reorientation in these materials. Figs. 4 (a, b) shows structures with a reoriented vdW gap for relaxed GaSe and $MoTe_2$ under pressure. Isosurface between layers indicates the presence of non-covalent interactions between layers. In the case of GaSe, under uniaxial pressure, a redistribution of interactions occurs, which determines the chain structure. A more detailed study of the connections between chains is the subject of our further research. During the relaxation process, the material again becomes quasi-two-dimensional and the vdW surface is restored again.

 https://www.doi.org/10.33910/2687-153X-2024-5-1-30-38

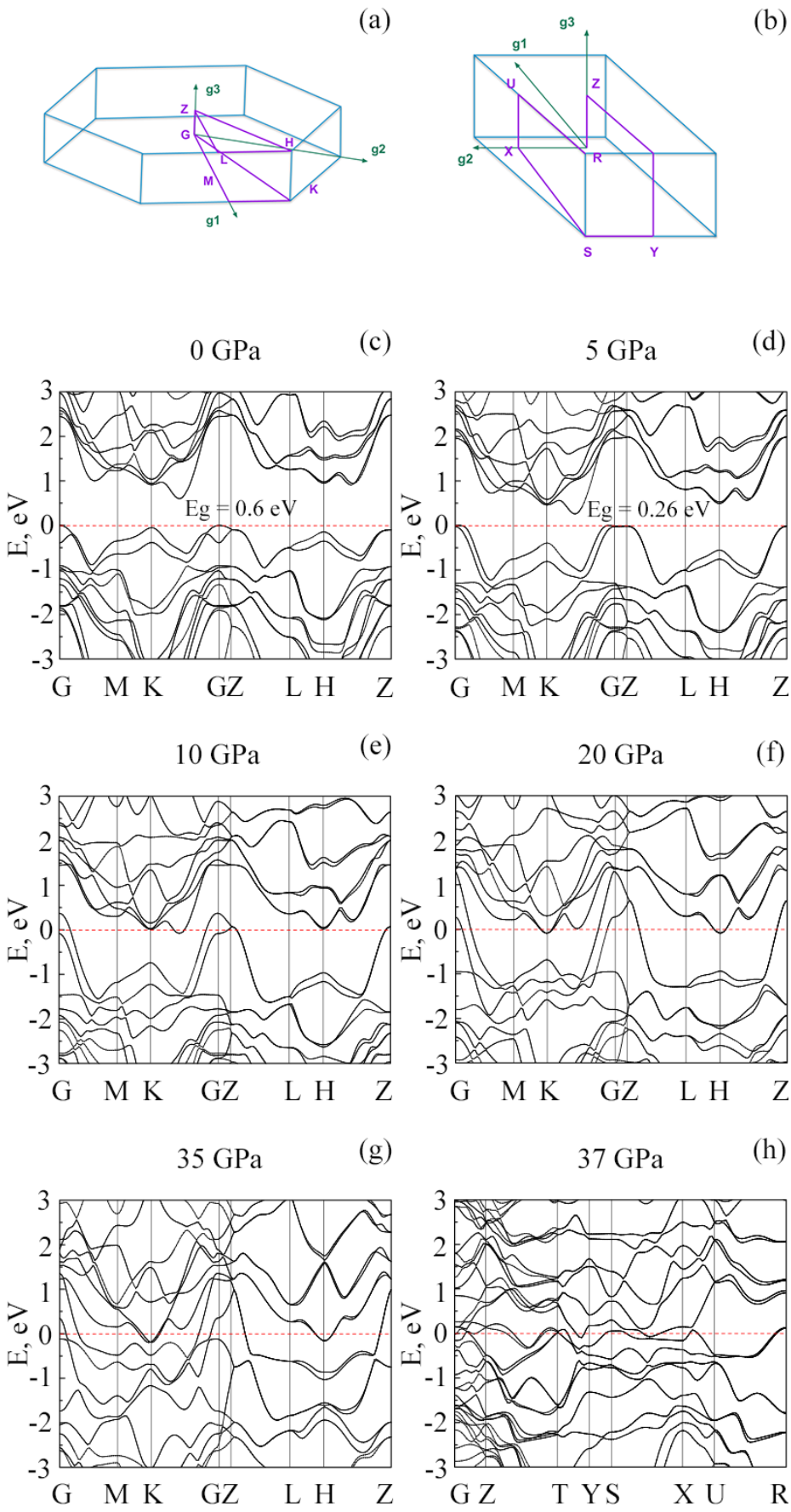

Fig. 2. Band structure patterns for $MoTe_2$ under different uniaxial pressures. (a)–(b) Brillouin zones for two phases (0 and 37 GPa). (c)–(h) Band structures for different pressure values

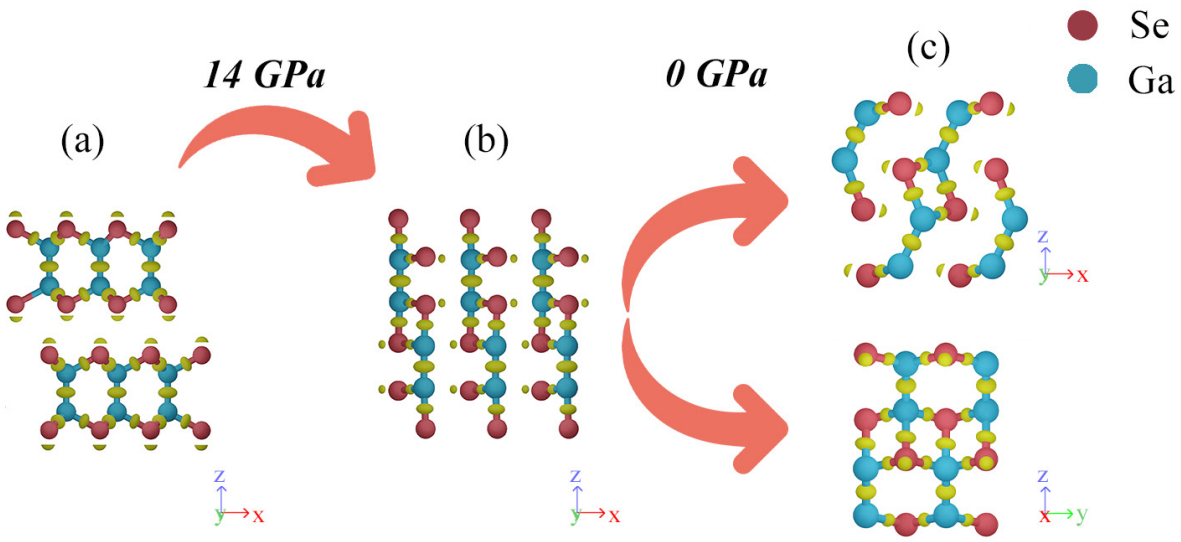

Fig. 3. Transformation of the GaSe structure under the influence of axial pressure and after releasing the pressure. (a) Initial structure, (b) New phase at 14 GPa, and (c) at a pressure of 0 GPa. Yellow balls represent CDD clouds

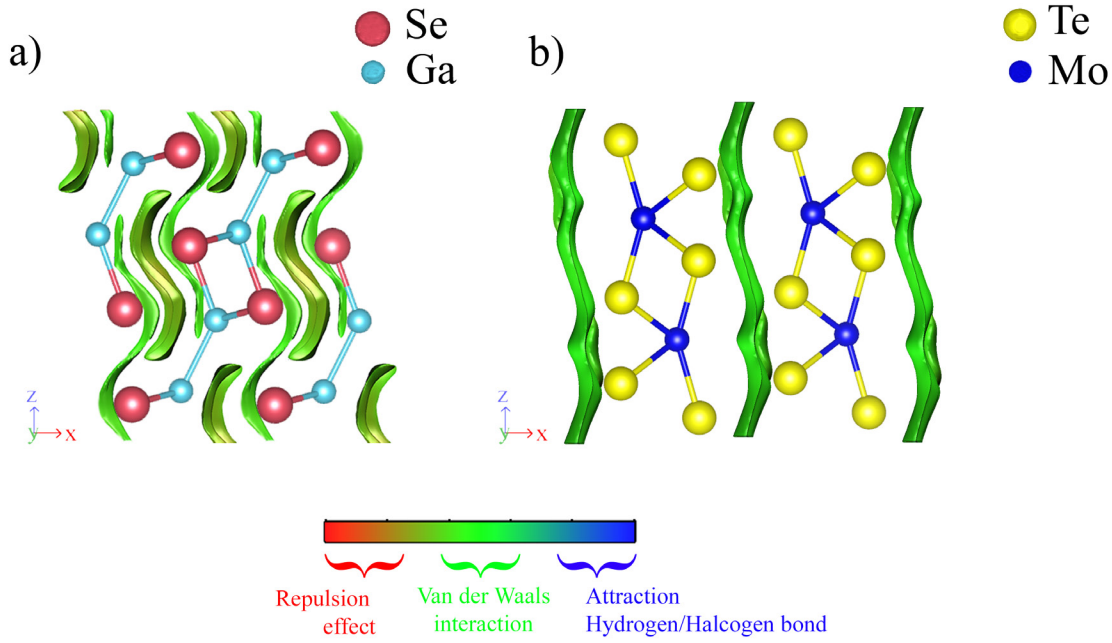

Fig. 4. RDG analysis of relaxed GaSe and $MoTe_2$ under pressure. Green isosurface shows the areas of vdW interaction

All of the above-mentioned classes of materials have one important common characteristic: the formation of a vdW gap, caused by additional CDD clouds associated with partial sp^3 hybridization of chalcogen atoms. Consequently, materials with similar CDD distributions are expected to exhibit similar vdW gap reconstruction patterns. For example, in graphite, which is known for the lack of additional density in the vdW gap, changes under pressure are significantly different. As for Sb_2Te_3, additional clouds of electron density in the gap are also observed in this material (Fig. 5 (a)). Despite that in the case of other materials (Figs. 1 and 3) these clouds undergo the transition to the new phase, but in the case of antimony telluride they retain their configuration and location in the new phase. Moreover, the question of the nature of interlayer interaction in Sb_2Te_3 remains unanswered, and there are reports that the connection between layers may be metavalent in nature (Zhang et al. 2023).

 https://www.doi.org/10.33910/2687-153X-2024-5-1-30-38

Under uniaxial pressure, antimony telluride undergoes a transition to a metallic state while preserving its layered structure. A further increase in pressure leads to a strong lateral displacement of the layers and a phase transition at 7 GPa (Fig. 5 (c)). In this case, the vdW gap disappears in the new phase. However, it is crucial to note that there are no bonds between the atoms through the gap; they possess lone pairs and engage in non-covalent interactions. Consequently, the closure of the gap is linked to the lateral sliding of the layers relative to each other along the vdW gap. This is distinct from the rearrangement of bonds seen in other layered materials.

When compared, the results at different pressures make it apparent that the impact of pressure on Sb_2Te_3 is mirrored in the band structure: bands at higher pressures exhibit slight broadening compared to those at lower pressures (Fig. 6 (c, d)). This aligns with heightened interactions between neighboring atoms, electrons, and orbitals resulting from a decreased interlayer distance.

Between pressures of 0 to 3 GPa (Fig. 6 (c, d)), the conduction band minimum (CBM) sharply decreases between points Γ and Z. The Valence Band Maximum (VBM) undergoes significant positional changes with pressure increase: at 0 GPa, it resides at point Γ, and with increasing pressure, it shifts from point Γ along the path to point M. By 3 GPa (Fig. 6 (d)), the CBM crosses the Fermi level, signifying metallization (Fig. 6 (e, f)) without undergoing a phase transition.

CDD analysis of the initial structures shows that the mechanism of interlayer interaction for all materials studied is determined to a large extent by the interaction between permanent dipoles, represented by the additional electron density in the vdW gap. When pressure is applied, all materials under study demonstrate different patterns of change in the vdW gap. In Sb_2Te_3, bonds inside the layer are not broken, and bonds through the gap arise due to the lateral displacement of the layers, without forming a vdW interaction plane, but creating regions with vdW interaction due to lone electron pairs.

At the same time, for GaSe and $MoTe_2$, the bonds inside the layer between the metal and chalcogen atoms are broken and arise through the vdW gap. Two-dimensional layers appear in $MoTe_2$, and quasi-one-dimensional chains appear in GaSe, and the symmetry of the cell in both these cases changes from hexagonal to orthorhombic. When GaSe relaxes, the symmetry does not increase and two-dimensional layers are formed with an orientation similar to the case of $MoTe_2$ (under pressure).

This leads to an important point: the vdW interaction does not disappear when axial pressure is applied. From the presented results it is obvious that, depending on the magnitude of intralayer interaction, coordination and local symmetry, the vdW gap can either rearrange ($MoTe_2$ and GaSe) or distribute, forming regions of non-covalent interaction, as seen in the example of Sb_2Te_3.

During relaxation of Sb_2Te_3, the regions of non-covalent interaction, due to an increase in symmetry, are united again into a single vdW surface. This result is consistent with the work of (Zheng et al. 2023),

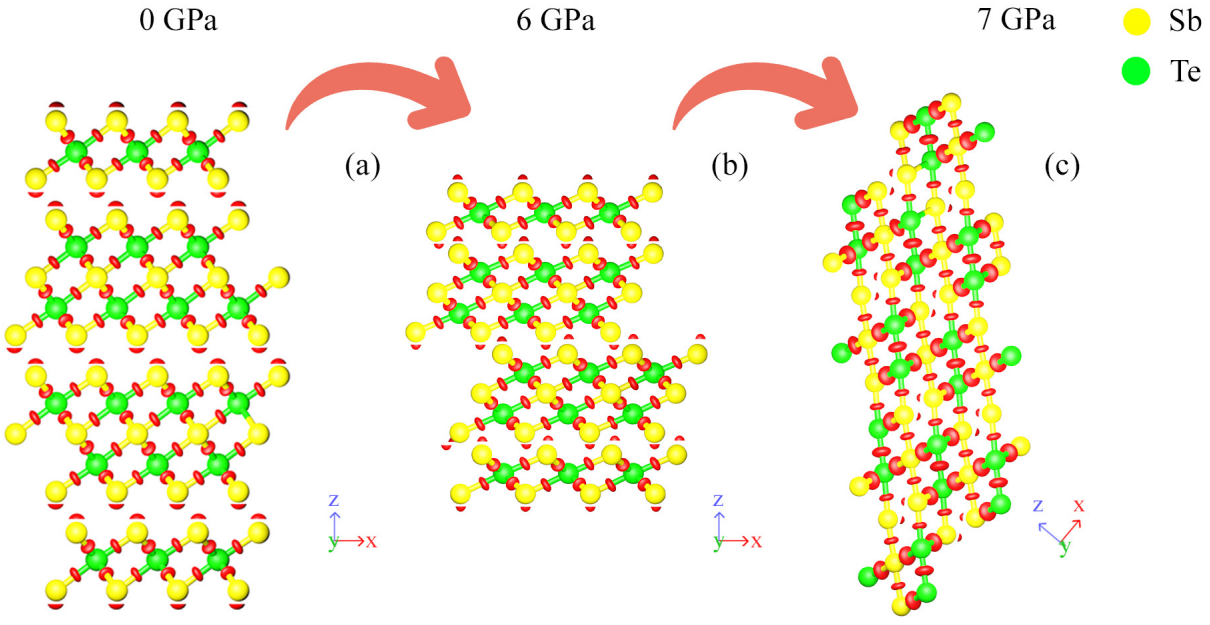

Fig. 5. Transformation of the Sb_2Te_3 structure under the axial pressure. (a) Initial structure, (b) Structure at 6 GPa before the phase transition, (c) New phase at 7 GPa. Red balls represent CDD clouds

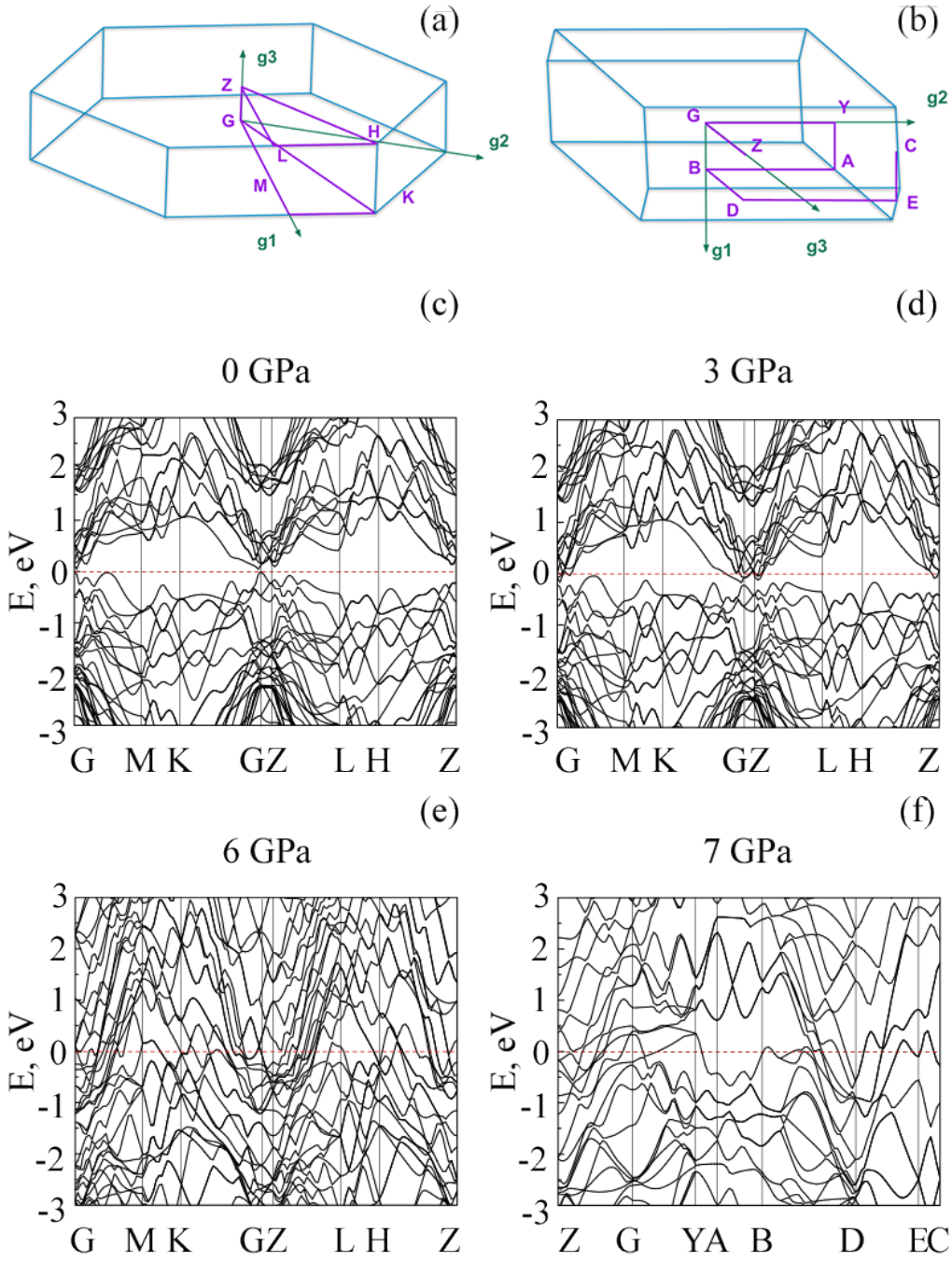

Fig. 6. Band structure patterns for Sb_2Te_3 under different uniaxial pressures. (a)–(b) Brillouin zones for two phases of Sb_2Te_3 (0 and 7 GPa). (c)–(e) Band structures for different pressure values

where it was shown that during the crystallization of Sb_2Te_3, the vdW gap is formed from vacancies (or, as we called it here, non-covalent interaction regions), which are pushed out in a correlated manner, forming a single defective surface — vdW surface.

Conclusions

It was shown that in $MoTe_2$, as in Sb_2Te_3, an isostructural phase transition associated with metallization occurs. It is shown that at a pressure of 37 GPa, a restructuring occurs in $MoTe_2$ with a change in the orientation of the vdW gap. Similar behavior is observed for the relaxed GaSe structure. For antimony telluride, the mechanism turned out to be different — it is associated with the redistribution of non-covalent interaction under the influence of axial pressure. In Sb_2Te_3, a phase transition occurs with

 https://www.doi.org/10.33910/2687-153X-2024-5-1-30-38

a change in symmetry due to the lateral sliding of the layers relative to each other, as a result of which a bulk structure with regions of non-covalent interaction is formed. It turned out that the symmetry and bond strength inside the layer play a significant role. Thus, it becomes possible to distinguish two mechanisms of destruction and formation of the vdW gap — with reconfiguration of the gap and redistribution of non-covalent interaction.

Conflict of Interest

The author declares that there is no conflict of interest, either existing or potential.

Acknowledgements

Author would like to express his sincere gratitude to Vasilisa Gerega, Anton Suslov, and Alexander Kolobov. Author is deeply appreciative of their insights, guidance, and comments, which have played a pivotal role in the successful completion of this work.

References

Barzilai, J., Borwein, J. M. (1988) Two-point step size gradient methods. *IMA Journal of Numerical Analysis*, 8(1), 141–148. https://doi.org/10.1093/imanum/8.1.141 (In English)

Benck, J. D., Hellstern, T. R., Kibsgaard, J. et al. (2014) Catalyzing the hydrogen evolution reaction (HER) with molybdenum sulfide nanomaterials. *Acs Catalysis*, 4 (11), 3957–3971. https://doi.org/10.1021/cs500923c (In English)

Bera, A., Singh, A., Gupta, S. N. et al. (2020) Pressure-induced isostructural electronic topological transitions in 2H-$MoTe_2$: X-ray diffraction and first-principles study. *Journal of Physics: Condensed Matter*, 33 (6), article 065402. https://doi.org/10.1088/1361-648X/abaeac (In English)

Bernevig, B. A. (2013) *Topological insulators and topological superconductors*. Princeton: Princeton University Press, 260 p. (In English)

Bernevig, B. A., Hughes, T. L., Zhang, S. C. (2006) Quantum spin Hall effect and topological phase transition in HgTe quantum wells. *Science*, 314 (5806), 1757–1761. https://www.science.org/doi/10.1126/science.1133734 (In English)

Chen, Y. L., Analytis, J. G., Chu, J.-H. et al. (2009) Experimental realization of a three-dimensional topological insulator, Bi_2Te_3. *Science*, 325 (5937), 178–181. https://doi.org/10.1126/science.1173034 (In English)

Clark, S. J., Segall, M. D., Pickard, C. J. et al. (2005) First principles methods using CASTEP. *Zeitschrift für Kristallographie-Crystalline Materials*, 220 (5-6), 567–570. https://doi.org/10.1524/zkri.220.5.567.65075 (In English)

Ernzerhof, M., Scuseria, G. E. (1999) Assessment of the Perdew–Burke–Ernzerhof exchange-correlation functional. *The Journal of Chemical Physics*, 110 (11), 5029–5036. https://doi.org/10.1063/1.478401 (In English)

Fan, X., Chang, C.-H., Zheng, W. T. et al. (2015) The electronic properties of single-layer and multilayer MoS_2 under high pressure. *The Journal of Physical Chemistry C*, 119 (19), 10189–10196. https://doi.org/10.1021/acs.jpcc.5b00317 (In English)

Gao, M.-R., Xu, Y.-F., Jiang, J., Yu, S.-H. (2013) Nanostructured metal chalcogenides: Synthesis, modification, and applications in energy conversion and storage devices. *Chemical Society Reviews*, 42 (7), 2986–3017. https://doi.org/10.1039/C2CS35310E (In English)

Grimme, S. (2006) Semiempirical GGA-type density functional constructed with a long-range dispersion correction. *Journal of Computational Chemistry*, 27 (15), 1787–1799. https://doi.org/10.1002/jcc.20495 (In English)

Grimme, S., Antony, J., Ehrlich, S., Krieg, H. (2010) A consistent and accurate ab initio parametrization of density functional dispersion correction (DFT-D) for the 94 elements H-Pu. *The Journal of Chemical Physics*, 132 (15). https://doi.org/10.1063/1.3382344 (In English)

Grimme, S., Ehrlich, S., Goerigk, L. (2011) Effect of the damping function in dispersion corrected density functional theory. *Journal of Computational Chemistry*, 32 (7), 1456–1465. https://doi.org/10.1002/jcc.21759 (In English)

Johnson, E. R., Keinan, S., Mori-Sánchez, P. et al. (2010) Revealing noncovalent interactions. *Journal of the American Chemical Society*, 132 (18), 6498–6506. https://doi.org/10.1021/ja100936w (In English)

Kane, C. L., Mele, E. J. (2005a) Quantum spin Hall effect in graphene. *Physical Review Letters*, 95 (22), article 226801. https://doi.org/10.1103/PhysRevLett.95.226801 (In English)

Kane, C. L., Mele, E. J. (2005b) Z_2 topological order and the quantum spin Hall effect. *Physical Review Letters*, 95 (14), article 146802. https://doi.org/10.1103/PhysRevLett.95.146802 (In English)

Konig, M., Wiedmann, S., Brune, C. et al. (2007). Quantum spin Hall insulator state in HgTe quantum wells. *Science*, 318 (5851), 766–770. https://doi.org/10.1126/science.1148047 (In English)

Lee, E., Kim, J., Bhoyate, S. et al. (2020) Realizing scalable two-dimensional MoS_2 synaptic devices for neuromorphic computing. *Chemistry of Materials*, 32 (24), 10447–10455. https://doi.org/10.1021/acs.chemmater.0c03112 (In English)

Lei, W., Wang, W., Ming, X. et al. (2020) Structural transition, metallization, and superconductivity in quasi-two-dimensional layered PdS2 under compression. *Physical Review B*, 101 (20), article 205149. https://doi.org/10.1103/PhysRevB.101.205149 (In English)

Li, P., Yuan, K., Lin, D.-Y. et al. (2019) p-MoS_2/n-InSe van der Waals heterojunctions and their applications in all-2D optoelectronic devices. *RSC Advances*, 9 (60), 35039–35044. https://doi.org/10.1039/C9RA06667E (In English)

Mu, C., Sun, X., Chang, Y. et al. (2021) High-performance flexible all-solid-state micro-supercapacitors based on two-dimensional InSe nanosheets. *Journal of Power Sources*, 482, article 228987. https://doi.org/10.1016/j.jpowsour.2020.228987 (In English)

Otero-de-la-Roza, A., Blanco, M. A., Pendás, A. M., Luaña, V. (2009) Critic: A new program for the topological analysis of solid-state electron densities. *Computer Physics Communications*, 180 (1), 157–166. https://doi.org/10.1016/j.cpc.2008.07.018 (In English)

Otero-de-la-Roza, A., Johnson, E. R., Luaña, V. (2014) Critic2: A program for real-space analysis of quantum chemical interactions in solids. *Computer Physics Communications*, 185 (3), 1007–1018. https://doi.org/10.1016/j.cpc.2013.10.026 (In English)

Pan, H., Cao, L., Chu, H. et al. (2019) Broadband nonlinear optical response of InSe nanosheets for the pulse generation from 1 to 2 μm. *ACS Applied Materials & Interfaces*, 11 (51), 48281–48289. https://doi.org/10.1021/acsami.9b18632 (In English)

Peng, X., Peng, L., Wu, C., Xie, Y. (2014) Two dimensional nanomaterials for flexible supercapacitors. *Chemical Society Reviews*, 43 (10), 3303–3323. https://doi.org/10.1039/C3CS60407A (In English)

Pumera, M., Sofer, Z., Ambrosi, A. (2014) Layered transition metal dichalcogenides for electrochemical energy generation and storage. *Journal of Materials Chemistry A*, 2 (24), 8981–8987. https://doi.org/10.1039/C4TA00652F (In English)

Qi, X.-L., Zhang, S.-C. (2011) Topological insulators and superconductors. *Reviews of Modern Physics*, 83 (4), article 1057. https://doi.org/10.1103/RevModPhys.83.1057 (In English)

Raty, J.-Y., Noé, P. (2020) Ovonic threshold switching in Se-Rich Ge_xSe_{1-x} glasses from an atomistic point of view: The crucial role of the metavalent bonding mechanism. *Physica Status Solidi (RRL)*, 14 (5), article 1900581. https://doi.org/10.1002/pssr.201900581 (In English)

Singh, B., Prasad, R. (2016) Spin-texture of the non-trivial surface state of topological insulator Sb_2Te_3. *Quantum Matter*, 5 (3), 362–364. https://doi.org/10.1166/qm.2016.1317 (In English)

Stepanov, R., Gerega, V., Suslov, A., Kolobov, A. (2023a) Uniaxial pressure-induced 2D–1D dimensionality change in GaSe and related materials. *Physica Status Solidi (RRL)*, 17 (8), article 2200430. https://doi.org/10.1002/pssr.202200430 (In English)

Stepanov, R. S., Marland, P. I., Kolobov, A. V. (2023b) Compositional and structural disorder in two-dimensional $A^{III}B^{VI}$ materials. *Crystals*, 13 (8), article 1209. https://doi.org/10.3390/cryst13081209 (In English)

Tominaga, J., Kolobov, A. V., Fons, P. J. et al. (2015) Giant multiferroic effects in topological GeTe-Sb_2Te_3 superlattices. *Science and Technology of Advanced Materials*, 16 (1), article 014402. https://doi.org/10.1088/1468-6996/16/1/014402 (In English)

Wang, H., Feng, H., Li, J. (2014) Graphene and graphene-like layered transition metal dichalcogenides in energy conversion and storage. *Small*, 10 (11), 2165–2181. https://doi.org/10.1002/smll.201303711 (In English)

Zhao, K., Wang, Y., Sui, Y. et al. (2015) First principles study of isostructural phase transition in Sb_2Te_3 under high pressure. *Physica Status Solidi (RRL)*, 9 (6), 379–383. https://doi.org/10.1002/pssr.201510091 (In English)

Zhao, X.-M., Liu, H.-Y., Goncharov, A. F. et al. (2019) Pressure effect on the electronic, structural, and vibrational properties of layered 2H – $MoTe_2$. *Physical Review B*, 99 (2), article 024111. https://doi.org/10.1103/PhysRevB.99.024111 (In English)

Zheng, Y., Song, W., Song, Z. et al. (2023) A complicated route from disorder to order in antimony-tellurium binary phase change materials. *Advanced Science*, article 2301021. https://doi.org/10.1002/advs.202301021 (In English)

Physics of Semiconductors.
Physics of thin films

UDC 538.935

EDN ZNCBNL
https://www.doi.org/10.33910/2687-153X-2024-5-1-39-43

The behavior of the optical characteristics of modified arsenic triselenide films

V. T. Avanesyan ✉[1]

[1] Herzen State Pedagogical University of Russia, 48 Moika Emb., Saint Petersburg 191186, Russia

Author

Vachagan T. Avanesyan, ORCID: 0000-0001-5772-8375, e-mail: avanesyan@mail.ru

For citation: Avanesyan, V. T. (2024) The behavior of the optical characteristics of modified arsenic triselenide films. *Physics of Complex Systems*, 5 (1), 39–43. https://www.doi.org/10.33910/2687-153X-2024-5-1-39-43 EDN ZNCBNL

Received 9 December 2023; reviewed 17 January 2024; accepted 17 January 2024.

Funding: The study did not receive any external funding.

Abstract: The influence of the level of modifier content on the behavior of the optical characteristics of thermally deposited films of arsenic triselenide chalcogenide glasses is investigated. A parallel shift of the absorption edge towards short wavelengths and a decrease in the slope of the exponential "tail" are observed. The increase in the slope of the Urbach energy dependence with an increasing modification level can be explained both by an increase in the concentration of metal-metal bonds, due to a deviation from stoichiometry, and by a transition through the value of the coordination number corresponding to the point of the topological phase transition. A simultaneous decrease in the band gap apparently indicates an increase in the defectiveness of the structure. In addition, it may indicate the presence of a higher concentration of trap states near the Fermi level, leading to a corresponding smearing in the "tails" of conductivity in chalcogenide glassy semiconductors (CGS).

Keywords: chalcogenide glasses, modifying impurity, absorption coefficient, Urbach energy, band gap

Introduction

Studying the influence of a modifying impurity on the optical properties of amorphous chalcogenide glasses in the As–Se system is important from the point of view of their use in optoelectronics (Avanesyan et al. 2022; Provotorov et al. 2021). The spectral dependence of optical absorption in amorphous semiconductors, as a rule, includes the following main regions:

1. Upper absorption region ($\alpha > 10^4$ cm^{-1}), in which the presence of interband transitions is assumed, and the absorption coefficient is determined by the following expression (Avanesyan et al. 2021):

$$\alpha(h\nu) = B(h\nu - E_g)^2 / h\nu \quad , \qquad (1)$$

where B is a constant, ν is the frequency of optical vibrations, h is Planck's constant, and E_g is the optical band gap. The latter is determined by the intersection of the tangent and the absorption curve in coordinates $\alpha(h\nu)^{1/2}$ with the axis of photon energy values $h\nu$.

2. Intermediate interval (1 cm^{-1}< α <10^4 cm^{-1}), in which parameter α depends exponentially on the photon energy, that is, the so-called "glassy" modification of Urbach's rule is performed (Weinstein et al. 2001):

$$\alpha(h\nu, T) = \alpha_{gl}\exp\left[\left(h\nu/E_U\right) + \left(T/T_o\right)\right], \quad (2)$$

where α_{gl} is a constant, E_U is a parameter (Urbach energy) which takes into account the degree of disorder present in the system and determines the width of the "tails" of the zones of localized states in the band gap, and T_o is the characteristic temperature. The temperature-independent logarithmic slope of the spectral response is given by:

$$1/E_U = \partial(\ln\alpha)/\partial(h\nu), \quad (3)$$

Expression (2) includes a shift of the absorption edge with increasing temperature to the long-wavelength region without changing the slope parameter E_U. The second term in the exponent (2) characterizes the linear temperature dependence of the absorption edge, which occurs in the temperature range from close to room temperature and above up to T_g. As some studies show, in the region of low temperatures there is a significant deviation from the linearity of the temperature shift of the optical edge. The parameter *E*u, proposed by Weinstein et al. (Weinstein et al. 2001), characterizes the influence of static (i. e., "frozen" phonons) and dynamic (i. e., thermal phonons) order disturbances arising from the movement of atoms from the equilibrium state. At the same time, this parameter is also a characteristic of the energy length of the band "tails" of the density of states. It was found that the specified parameter is highly sensitive to changes in the structure and level of order, making it an ideal tool for obtaining information about structural changes in glass caused by various experimental conditions. Unfortunately, there is no unambiguous interpretation of the nature of the rule under discussion. There are usually three main factors that determine the value of the E_U parameter for glassy semiconductors (Sobolev 2012): a) the dominant type of the chemical bond, b) coordination number of the glass former, c) the size of atoms in the modifier sublattice.

3. Weak absorption in the "tails" of the zones with a low value of the coefficient $\alpha < 1$ cm^{-1}, whose shape of dependence and value are determined by the degree of purification, thermal history and sample manufacturing technology.

Experimental methods

The behavior of impurities in amorphous semiconductors raises two issues — one related to the nature of defects and the other, to the degree of disorder. In thermally deposited CGS films, the structure of which is more disordered than in bulk samples, the addition of modifier atoms occurs more easily. Films for optical measurements were prepared by vacuum deposition of the original CGS onto a glass substrate kept at room temperature. The degree of amorphism of the studied samples was controlled by the X-ray method. Optical absorption was measured using an SF-2000 and SF-56 spectrophotometer. The incident radiation was perpendicular to the surface of the layer under study.

Results and discussion

Fig. 1 shows the spectral characteristics of the absorption coefficient α of As_2Se_3 films obtained by vacuum deposition for different levels of modifying impurity (Pb) content. The data obtained indicate a parallel shift of the absorption edge with increasing Pb content, a shift of the spectrum towards shorter wavelengths, and a decrease in the slope of the exponential tail with increasing modifier content. In this case, the highest slope corresponded to undoped CGS. The intermediate value of the absorption coefficient complies with Urbach's rule, which is usually associated with a superposition of electron transitions from the "tails" of the valence band to the states of the extended conduction band. There is a simple correlation between the apparent band gap and the width of the valence band "tail" E_o (Vainshtein et al. 2000):

$$E_g = E_{go} - cE_o, \quad (4)$$

where E_{go} is the maximum band gap for an infinitesimal tail width, and c is a constant.

If the width of the Urbach tail varies with impurity concentration (or temperature), extrapolating the Eu energy edges to the high energy region for different amounts of impurities gives an intercept

 https://www.doi.org/10.33910/2687-153X-2024-5-1-39-43

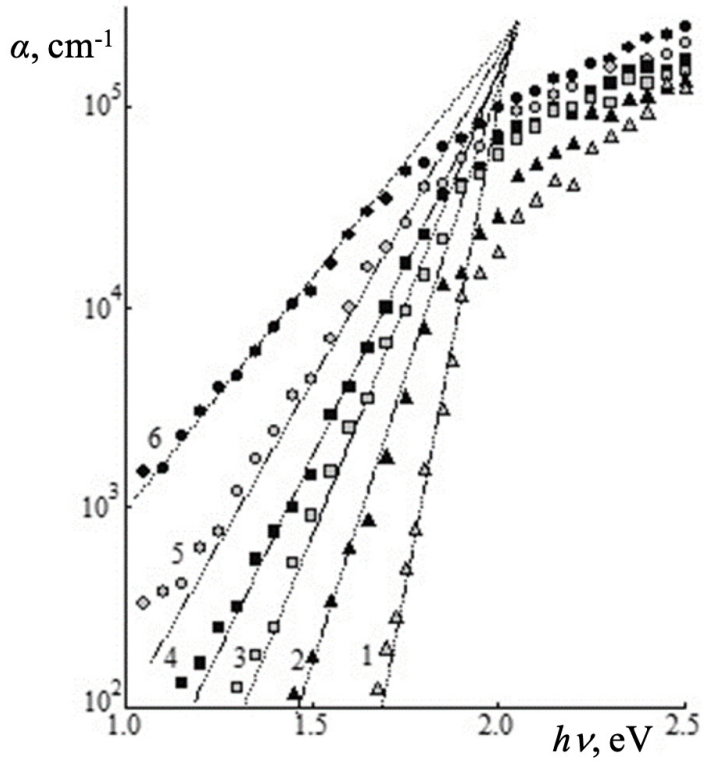

Fig. 1. Absorption spectra of As_2Se_3<Pb> films with different levels of modifier content: 1 — undoped sample, 2 — 1.5 %, 3 — 3.2 %, 4 — 4.1 %, 5 — 6.4 %, 6 — 10.5 at. % Pb

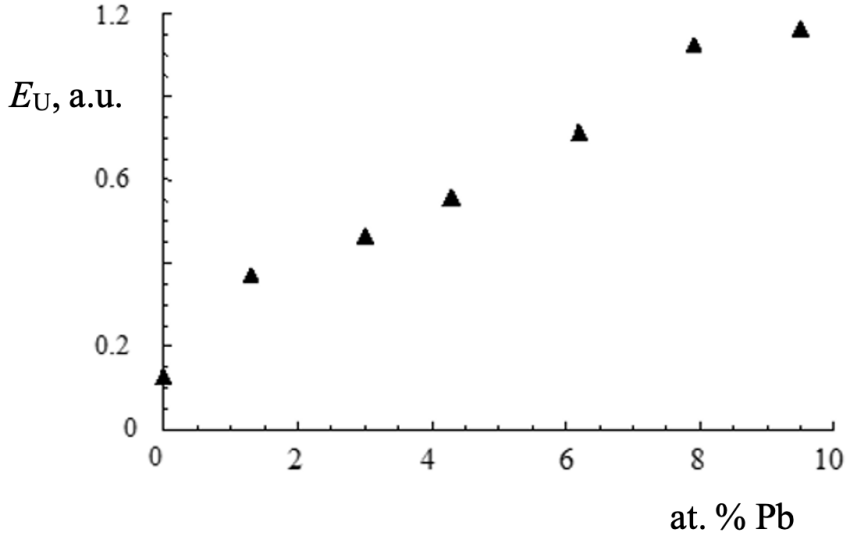

Fig. 2. Dependence of Urbach energy on the percentage of the modifier for As_2Se_3 <Pb>

corresponding to the value of E_{go}. Fig. 2 shows the dependence of the Urbach energy E_U on the level of modification of the samples of the CGS under study. Two areas of increasing E_U value can be noted. As the modifier content increases, the slope of the dependence becomes steeper. The observed increase in E_U values, as shown by previous studies, can be explained by two reasons, namely: a) an increase in the concentration of metal-to-metal bonds due to a deviation from stoichiometry, b) a transition through the value of the coordination number corresponding to the point of topological phase transition. The observed expansion of the Urbach "tail" may be associated with an increase in disorder during the formation of new structural elements in combination with modifier atoms in addition to the existing structural disorder.

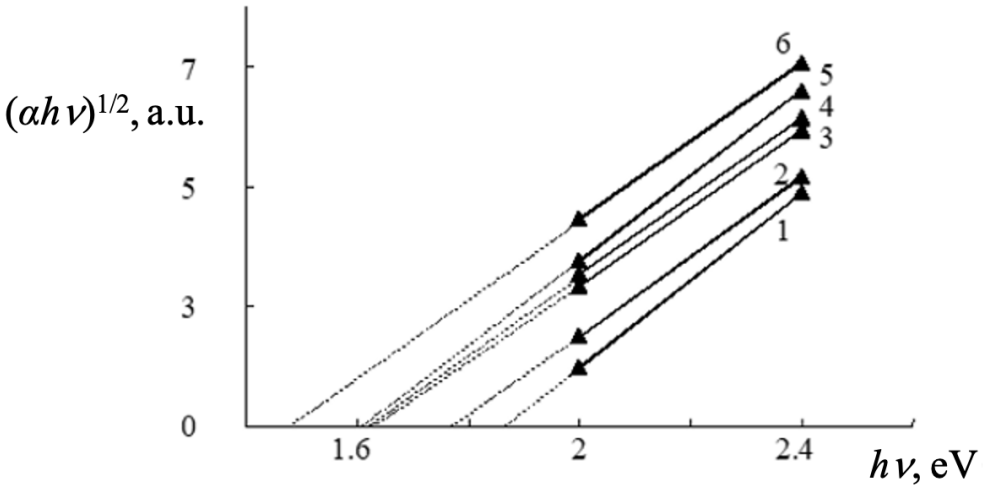

Fig. 3. Tauc plot for modified As_2Se_3<Pb> films (linear approximation):
1 — 0, 2 — 1.5, 3 — 3.2, 4 — 4.1, 5 — 6.4, 6 — 10.5 at. % Pb

Fig. 3 shows the corresponding dependences in Tauc coordinates (Tauc 1968) for As_2Se_3 film structures.

The optical band gap E_g was determined by extrapolating the linear dependence of the optical absorption edge from the $\alpha^2(h\nu)$ curves. The data obtained show a decrease in this parameter proportional to the percentage of impurities. The decrease in E_g with increasing Pb content is in satisfactory agreement with the results of studies on the effect of doping on the optical properties of CGS obtained by other authors. The difference in the value of the band gap apparently indicates a greater defectiveness of the structure and, probably, a greater concentration of trap states near the Fermi level, which leads to a corresponding smearing in the "tails" of CGS conductivity. Following the fact that the Pb–Se bond energy is greater than the As–Se one, we can conclude that the concentration of As–As bonds increases with increasing modifier content. The noted behavior of the Tauc plots can be determined by the formation of new structural units of the PbSe type, which accompanies the introduction of the modifier and reduces the optical band gap compared to the original matrix.

The structure of As_2Se_3 is usually represented using a statistical model based on structural units — clusters of the AsSe, $AsSe_2As$, $AsSeAs_2$ and $AsAs_3$ types. The AsSe compound is dominated by molecular fragments As_2Se_3 and As_4Se_4 with the presence of homobonds between arsenic atoms. These bonds lead to a noticeable decrease in the binding energy in the AsSe lattice compared to stoichiometric As_2Se_3. Under these conditions, the formation of new clusters based on impurity atoms (for example, PbSe) does not contradict the structural model. Apparently, both factors contribute to the observed behavior of the E_U parameter. The increase in the slope of the E_U dependence may be associated with a topological phase transition to a layered structure. According to available data, the energy states near the valence band of the As_2Se_3 material mainly include the p-orbitals of chalcogen lone pairs (low-energy region of the reflection region), and the high-energy maximum zone belongs to the pσ orbital of the chalcogen atom. The p and s As orbitals contribute to both sides of the reflectance spectrum peak.

Conclusions

The conducted studies show that the addition of a modifier significantly modifies the fundamental reflection spectrum of CGS based on the As–Se systems, lowering the low-energy branch and raising the high-energy side of the spectral reflection curve. These changes indicate an increase in the role of bonding orbitals compared to the contribution of orbitals belonging to lone electron pairs. It has been established that the key physical and, in particular, optical characteristics of chalcogenide glasses are closely related to the presence of LEP in chalcogens involved in the formation of the upper part of the valence band of the semiconductor. Chalcogenide lone pair semiconducting materials are important due to their prospective applications in thermoelectrics, phase change memories, topological insulators, etc. At a low percentage of Pb, one can expect a stronger influence of impurity on intermolecular interactions

 https://www.doi.org/10.33910/2687-153X-2024-5-1-39-43

since delocalization of lone pair electrons reduces the energy of valence states and contributes to stabilization of the entire structure.

Conflict of Interest

The author declares that there is no conflict of interest, either existing or potential.

References

Avanesyan, V. T., Provotorov, P. S., Krbal, M., Kolobov, A. V. (2022) Optical characteristics of modified $As_{30}S_{70}$ thin films. *Physics of Complex Systems*, 3 (3), 137–143. https://www.doi.org/10.33910/2687-153X-2022-3-3-137-143 (In English)

Avanesyan, V. T., Provotorov, P. S., Stozharov, V. M. et al. (2021) Spectroscopy of zinc oxide thin films near the fundamental absorption edge. *Optics and Spectroscopy*, 129 (11), 1196–1199. https://doi.org/10.1134/S0030400X21090046 (In English)

Provotorov, P. S., Avanesyan, V. T., Krbal, M., Kolobov, A. V. (2021) Effect of doping of molybdenum on the optical properties of glasses of the As–S system. *Physics of Complex Systems*, 2 (3), 115–121. https://www.doi.org/10.33910/2687-153X-2021-2-3-115-121 (In English)

Sobolev, V. V. (2012) *Opticheskie svojstva i elektronnaya struktura nemetallov: vvedenie v teoriyu [Optical properties and electronic structure of nonmetals: Introduction to theory]*. Izhevsk: Izhevsk Institute of Computer Research Publ., 584 p. (In Russian)

Tauc, J. (1968) Opticheskie svojstva poluprovodnikov v vidimoj i ul'trafioletovoj oblastyakh spektra [Optical properties of semiconductors in the visible and ultraviolet regions of the spectrum]. *Uspekhi fizicheskikh nauk — Advances in Physical Sciences*, 9 (3), 501–534. https://doi.org/10.3367/UFNr.0094.196803e.0501 (In Russian)

Vainshtein, I. A., Zatsepin, A. F., Kortov, V. S., Shchapova, Yu. V. (2000) The Urbach rule for the $PbO\text{-}SiO_2$ glasses. *Physics of the Solid State*, 42 (2), 230–235. https://doi.org/10.1134/1.1131151 (In English)

Weinstein, I. A., Zatsepin, A. F., Kortov, V. S. (2001) Effects of structural disorder and Urbach's rule in binary lead silicate glasses. *Journal of Non-Crystalline Solids*, 279 (1), 77–87. https://doi.org/10.1016/S0022-3093(00)00396-3 (In English)

Summaries in Russian / Информация о статьях на русском языке

Физика конденсированного состояния

ТРЕХФОТОННОЕ ПОГЛОЩЕНИЕ СВЕТА И ФОТОЛЮМИНЕСЦЕНЦИЯ В ПЛЕНКАХ ЖИДКОКРИСТАЛЛИЧЕСКИХ ПОЛИМЕРОВ С ВНЕДРЕННЫМИ КВАНТОВЫМИ ТОЧКАМИ CdSe/ZnS

Вячеслав Юрьевич Нестеров, Никита Денисович Преснов, Станислав Васильевич Заботнов, Алексей Сократович Мерекалов, Олег Николаевич Карпов, Георгий Александрович Шандрюк, Раиса Викторовна Тальрозе, Леонид Анатольевич Головань

Аннотация. В данной работе исследовано нелинейное поглощение инфракрасных (ИК) (1250 нм) фемтосекундных импульсов и возбуждаемая ими видимая фотолюминесценция (ФЛ) в жидкокристаллических (ЖК) полимерных пленках с внедренными квантовыми точками (КТ) CdSe/ZnS типа «ядро–оболочка». Зависимость нелинейного пропускания от падающей интенсивности указывает на трехфотонное поглощение в пленках, при этом коэффициент поглощения трех фотонов для полимерного композита КТ–ЖК полимер сопоставим с этой величиной для объемного CdSe. Спектр ФЛ, возбуждаемой ИК-импульсами, совпадает со спектром однофотонной ФЛ. Зависимость сигнала ФЛ от мощности излучения ИК-лазера кубическая с последующим насыщением для спектрального диапазона 2,10–2,25 эВ, при этом интенсивность насыщения уменьшается для меньшей энергии фотонов ФЛ. Присутствие сигнала второй гармоники в спектре сигнала ап-конверсии приводит к его изменению с увеличением мощности возбуждения.

Ключевые слова: полупроводниковые квантовые точки, жидкокристаллический полимер, ап-конверсия, фотолюминесценция, многофотонное поглощение

Для цитирования: Nesterov, V. Yu., Presnov, N. D., Zabotnov, S. V., Merekalov, A. S., Karpov, O. N., Shandryuk, G. A., Talroze, R. V., Golovan, L. A. (2024) Three-photon absorption and photoluminescence in films of liquid-crystal polymers with embedded CdSe/ZnS quantum dots. *Physics of Complex Systems*, 5 (1), 3–9. https://www.doi.org/10.33910/2687-153X-2024-5-1-3-9 EDN LFAWTO

ДИЭЛЕКТРИЧЕСКИЕ СВОЙСТВА ФОТОАНОДОВ ДЛЯ СЕНСИБИЛИЗИРОВАННЫХ СОЛНЕЧНЫХ ЭЛЕМЕНТОВ

Екатерина Владимировна Текшина, Петр Иванович Лазаренко, Александр Сергеевич Степарук, Дарья Алексеевна Крупанова, Сергей Александрович Козюхин

Аннотация. Исследования солнечной энергии актуальны особенно в области изучения и создания сенсибилизированных красителей солнечных элементов (СКСЭ), относящихся к третьему поколению фотовольтаических преобразователей солнечного света. Перспективным направлением является создание архитектурных и интерьерно-интегрированных панелей, гибких и портативных устройств. Изучение свойств функциональных материалов, входящих в структуру СКСЭ, и их влияния друг на друга имеет решающее значение для повышения эффективности, снижения себестоимости производства СКСЭ.

В работе исследованы диэлектрические свойства фотоанодов (ФА) для СКСЭ, в частности, диэлектрическая проницаемость и тангенс диэлектрических потерь в диапазоне от –50 до 150 °C и от 10^{-1}–10^{6} Гц, что позволило оценить вклад красителя в диэлектрические свойства диоксида титана.

Полученные результаты позволяют понять влияние красителя на механизм проводимости носителей заряда в диоксиде титана и могут быть использованы при разработке материалов для СКСЭ.

Ключевые слова: диэлектрические свойства, мезопористый слой, диоксид титана, солнечная энергетика, солнечные элементы, композитные материалы

Для цитирования: Tekshina, E. V., Lazarenko, P. I., Steparuk, A. S., Krupanova, D. A., Kozyukhin, S. A. (2024) Dielectric properties of photoanodes for dye-sensitized solar cells. *Physics of Complex Systems*, 5 (1), 10–17. https://www.doi.org/10.33910/2687-153X-2024-5-1-10-17 EDN GUXCPV

К ОЦЕНКЕ ПРЕДЕЛЬНЫХ ВОЗМОЖНОСТЕЙ ТЕРМОЭЛЕКТРИЧЕСКОГО ПРЕОБРАЗОВАНИЯ ЭНЕРГИИ

Владимир Минович Грабов, Владимир Алексеевич Комаров, Василиса Александровна Герега, Антон Владимирович Суслов

Аннотация. На основе термодинамического соотношения между коэффициентом термоэдс и энтропией электропроводящей среды для электронной системы полностью ионизованной плазмы, находящейся в наиболее неупорядоченном состоянии, природным примером которой может служить электронно-ядерная плазма Солнца, получено оценочное значение параметра термоэлектрической эффективности ZT, выражающееся универсальным числом ZT = (25/6), которое можно рассматривать как некоторую оценку предельных возможностей термоэлектрического преобразования энергии.

Ключевые слова: термоэлектричество, наиболее неупорядоченное состояние электронной системы, плазма Солнца, безразмерный параметр термоэлектрической эффективности ZT, предельное значение ZT

Для цитирования: Grabov, V. M., Komarov, V. A., Gerega, V. A., Suslov, A. V. (2024) Thermoelectric energy conversion: Assessment of limiting capabilities. *Physics of Complex Systems*, 5 (1), 18–20. https://www.doi.org/10.33910/2687-153X-2024-5-1-18-20 EDN VRRAMV

Теоретическая физика

МЕТОД ГИПЕРБОЛИЧЕСКИХ МАТРИЦ ДЛЯ ИССЛЕДОВАНИЯ ДИНАМИКИ АТОМОВ И МОЛЕКУЛ С ПОМОЩЬЮ ВОЛНОВЫХ ПАКЕТОВ

Максим Юрьевич Яковлев, Андрей Константинович Беляев

Аннотация. Метод гиперболических матриц предложен для исследования ядерной динамики атомов и молекул в рамках техники волновых пакетов и формализма подхода Борна — Оппенгеймера. Метод позволяет рассчитывать эволюцию волнового пакета при помощи произведения обычных матриц вместо распространения во времени посредством матричных экспонент. Формализм метода подробно описан, и представлен иллюстративный пример применения метода к модели Талли. Получено хорошее согласие с результатами применения модели Ландау — Зинера.

Ключевые слова: волновой пакет, атомные и молекулярные столкновения, неадиабатические переходы, ядерная динамика, матричная экспонента

Для цитирования: Yakovlev, M. Yu., Belyaev, A. K. (2024) The hyperbolic matrix method for wave packet treatment of atomic and molecular dynamics. *Physics of Complex Systems*, 5 (1), 21–29. https://www.doi.org/10.33910/2687-153X-2024-5-1-21-29 EDN UBYSBH

Физика полупроводников

ВЛИЯНИЕ ОДНООСНОГО ДАВЛЕНИЯ НА СТРУКТУРНЫЕ И ЭЛЕКТРОННЫЕ СВОЙСТВА ДВУМЕРНЫХ МАТЕРИАЛОВ НА ПРИМЕРЕ $MoTe_2$ И Sb_2Te_3

Роман Сергеевич Степанов

Аннотация. Это исследование сосредоточено на моделировании методами DFT воздействия одноосного давления на электронные и структурные характеристики двумерных материалов, таких как $MoTe_2$ и Sb_2Te_3. Особое внимание уделяется реконфигурации щели ван-дер-Ваальса (вдВ). Интуитивно, при приложении одноосного давления ожидается уменьшение расстояния между слоями и, как следствие, переход 2D–3D. Моделирование Sb_2Te_3 под одноосным давлением выявило металлизацию при 3 ГПа. Дополнительное увеличение давления вызывает изменение симметрии и фазовый переход при 7 ГПа, что приводит к исчезновению щели вдВ в новой фазе. Тем не менее переход к объемной фазе не всегда происходит. В случае $MoTe_2$ под воздействием давления происходит изоструктурный переход в металлическое состояние при 10 ГПа. Дальнейшее увеличение давления при 37 ГПа вызывает фазовый переход с реконфигурацией щели вдВ. Важно отметить, что данный случай $MoTe_2$ аналогичен ситуации с GaSe после релаксации, что также является предметом данного исследования.

Ключевые слова: 2D полупроводники, ван-дер-Ваальсово взаимодействие, DFT, одноосное давление, $MoTe_2$, Sb_2Te_3, структурные превращения

Для цитирования: Stepanov, R. S. (2024) Uniaxial pressure modulation of two-dimensional materials: Insights into the structure and electronic properties of $MoTe_2$ and Sb_2Te_3. *Physics of Complex Systems*, 5 (1), 30–38. https://www.doi.org/10.33910/2687-153X-2024-5-1-30-38 EDN SUQFNX

ПОВЕДЕНИЕ ОПТИЧЕСКИХ ХАРАКТЕРИСТИК МОДИФИЦИРОВАННЫХ ПЛЕНОК ТРИСЕЛЕНИДА МЫШЬЯКА

Вачаган Тигранович Аванесян

Аннотация. Исследовано влияние уровня содержания модификатора на поведение оптических характеристик термически осажденных пленок халькогенидных стекол триселенида мышьяка. Наблюдается параллельный сдвиг края поглощения в сторону коротких волн и уменьшение наклона экспоненциального «хвоста». Увеличение наклона энергетической зависимости Урбаха с увеличением степени модификации можно интерпретировать как увеличение концентрации связей металл-металл за счет отклонения от стехиометрии, так и переходом через значение координационного числа, соответствующего точке топологического фазового перехода. Одновременное уменьшение ширины запрещенной зоны указывает, по-видимому, на увеличение дефектности структуры. Кроме того, это может свидетельствовать о наличии более высокой концентрации ловушечных состояний вблизи уровня Ферми, приводящей к соответствующему размытию «хвостов» проводимости халькогенидных стеклообразных полупроводников (ХСП).

Ключевые слова: халькогенидные стекла, модифицирующая примесь, коэффициент поглощения, энергия Урбаха, запрещенная зона

Для цитирования: Avanesyan, V. T. (2024) The behavior of the optical characteristics of modified arsenic triselenide films. *Physics of Complex Systems*, 5 (1), 39–43. https://www.doi.org/10.33910/2687-153X-2024-5-1-39-43 EDN ZNCBNL